Monthly Notices of the ROYAL ASTRONOMICAL SOCIETY

MNRAS **534,** 151–172 (2024) https://doi.org/10.1093/mnras/stae2048
Advance Access publication 2024 August 31

The cosmic rate of pair-instability supernovae

Francesco Gabrielli,[1,2]★ Andrea Lapi ,[1,2,3,4] Lumen Boco,[1,2,3] Cristiano Ugolini,[1,5] Guglielmo Costa ,[6] Cecilia Sgalletta,[1,7] Kendall Shepherd,[1,8] Ugo N. Di Carlo,[1] Alessandro Bressan,[1] Marco Limongi[5,9,10] and Mario Spera[1,2,5]

[1]*SISSA, via Bonomea 265, I-34136 Trieste, Italy*
[2]*National Institute for Nuclear Physics – INFN, Sezione di Trieste, I-34127 Trieste, Italy*
[3]*Institute for Fundamental Physics of the Universe – IFPU, Via Beirut 2, I-34014 Trieste, Italy*
[4]*Istituto di Radioastronomia – INAF/IRA, Via Piero Gobetti 101, I-40129 Bologna, Italy*
[5]*Istituto Nazionale di Astrofisica – Osservatorio Astronomico di Roma, Via Frascati 33, I-00040, Monteporzio Catone, Italy*
[6]*Univ Lyon1, ENS de Lyon, CNRS, Centre de Recherche Astrophysique de Lyon, UMR5574, F-69230 Saint-Genis-Laval, France*
[7]*INFN – Padova, Via Marzolo 8, I-35131 Padova, Italy*
[8]*INAF – Osservatorio Astronomico di Padova, Vicolo dell'Osservatorio 5, I-35122 Padova, Italy*
[9]*Kavli Institute for the Physics and Mathematics of the Universe, Todai Institutes for Advanced Study, University of Tokyo, Kashiwa, 277-8583, Japan*
[10]*INFN, Sezione di Perugia, via A. Pascoli s/n, I-06125 Perugia, Italy*

Accepted 2024 August 27. Received 2024 August 7; in original form 2024 May 4

ABSTRACT

Pair-instability supernovae (PISNe) have crucial implications for many astrophysical topics, including the search for very massive stars, the black hole mass spectrum, and galaxy chemical enrichment. To this end, we need to understand where PISNe are across cosmic time, and what are their favourable galactic environments. We present a new determination of the PISN rate as a function of redshift, obtained by combining up-to-date stellar evolution tracks from the PARSEC and FRANEC codes, with an up-to-date semi-empirical determination of the star formation rate and metallicity evolution of star-forming galaxies throughout cosmic history. We find the PISN rate to exhibit a huge dependence on the model assumptions, including the criterion to identify stars unstable to pair production, and the upper limit of the stellar initial mass function. Remarkably, the interplay between the maximum metallicity at which stars explode as PISNe, and the dispersion of the galaxy metallicity distribution, dominates the uncertainties, causing a $\sim$ seven-orders-of-magnitude PISN rate range. Furthermore, we show a comparison with the core-collapse supernova rate, and study the properties of the favourable PISN host galaxies. According to our results, the main contribution to the PISN rate comes from metallicities between $\sim 10^{-3}$ and 10^{-2}, against the common assumption that views very low metallicity, Population III stars as exclusive or dominant PISN progenitors. The strong dependencies we find offer the opportunity to constrain stellar and galaxy evolution models based on possible future (or the lack of) PISN observations.

Key words: stars: evolution – galaxies: general – transients:supernovae.

1 INTRODUCTION

Pair-instability supernovae (PISNe) are explosions that develop inside the cores of very massive stars (VMSs) at the end of their evolution, leading to the complete disruption of the progenitor. The physical mechanism behind PISNe has been well understood ever since its discovery (Fowler & Hoyle 1964; Barkat, Rakavy & Sack 1967; Bisnovatyi-Kogan & Kazhdan 1967; Rakavy & Shaviv 1967; Fraley 1968). At the end of C burning in the core, where temperatures approach 10^9 K and densities are greater than ~ 100 g cm^{-3}, photons become energetic enough to create electron–positron pairs. The pair-production process removes radiation pressure, which counteracts the gravitational pull from the inner layers, and lowers the adiabatic index Γ below 4/3. As a result, the star becomes unstable and begins to collapse in a runaway fashion. The onset of explosive O and Si burning releases energies of $\sim 10^{52} - 10^{53}$ erg (Heger & Woosley 2002), high enough to eject all the star's material, without leaving any remnant behind. The explosion produces high amounts of ^{56}Ni, up to $\gtrsim 50$ M$_\odot$ (Heger & Woosley 2002). Its radioactive decay is held responsible for luminosities up to 10^2 times those of typical core-collapse supernovae (CCSNe, e.g. Scannapieco, Schneider & Ferrara 2003; Kasen, Woosley & Heger 2011; Dessart et al. 2012; Whalen et al. 2013; Kozyreva et al. 2014a, 2016; Kozyreva, Yoon & Langer 2014b; Jerkstrand, Smartt & Heger 2015; Smidt et al. 2015; Gilmer et al. 2017; Hartwig, Bromm & Loeb 2018; Chatzopoulos et al. 2019). Despite PISNe being so luminous, and the several hundreds of CCSN observations achieved so far (e.g. Cooke et al. 2012; Yaron & Gal-Yam 2012; Gal-Yam et al. 2013; Guillochon et al. 2017), no PISN has ever been confidently discovered. Several candidate detections have been reported, including superluminous supernovae (SLSNe), but none has been confirmed as a PISN (Woosley, Blinnikov &

★ E-mail: fgabriel@sissa.it

Heger 2007; Gal-Yam et al. 2009; Quimby et al. 2011; Cooke et al. 2012; Gal-Yam 2012; Kozyreva & Blinnikov 2015; Lunnan et al. 2016; Kozyreva et al. 2018; Gomez et al. 2019; Mazzali et al. 2019; Nicholl et al. 2020; Schulze et al. 2024).

PISNe are predicted to occur in stars with masses on the zero-age main sequence (ZAMS) in the range $140 \lesssim M_{\rm ZAMS}/{\rm M}_{\odot} \lesssim 260$, and metallicities ($Z$) below some threshold (Heger & Woosley 2002; Heger et al. 2003). Stars undergo pair instability starting from $M_{\rm ZAMS} \sim 100\,{\rm M}_{\odot}$, but below $\sim$140 $\rm M_{\odot}$ they experience a series of pulsations, accompanied by the ejection of the most external layers, in a pulsational pair-instability supernova (PPISN, Heger & Woosley 2002; Heger et al. 2003). In this case, the core stays mostly intact, and the star finally collapses into a black hole (BH). Above $\sim$ 140 $\rm M_{\odot}$, the first pulsation is so energetic that it completely disrupts the star. For masses higher than $\sim$ 260 $\rm M_{\odot}$, the star directly collapses into an intermediate-mass BH (Heger & Woosley 2002; Heger et al. 2003). If Z is too high, mass loss due to stellar winds prevents the star from forming cores massive enough to become unstable (Heger et al. 2003). The maximum metallicity at which stars explode as PISNe is uncertain. Stellar evolution simulations succeed in producing PISNe up to some fraction of the solar metallicity, generally below $\sim 0.5\,Z_{\odot}$ (Langer et al. 2007; Langer 2012; Kozyreva et al. 2014b; Spera & Mapelli 2017; Costa et al. 2021; Higgins et al. 2021; Martinet et al. 2023; Sabhahit et al. 2023).

Stellar evolution codes simulate the evolution of stars from the ZAMS throughout the nuclear burning stages, providing a link between $M_{\rm ZAMS}$ and the final core mass, at the pre-SN stage. In order to identify stars undergoing pair instability, it is common to adopt a criterion based on the final mass of the core. As described above, the physical processes behind the onset of instability are much more complex. None the less, the core mass criterion represents a good and useful proxy. By assuming that stars with He or CO core mass in a certain range end their life as PISN, it is possible to obtain a range of PISN progenitor masses. Depending on the details of the adopted stellar evolution code, the $M_{\rm ZAMS}$ range where PISNe occur can fluctuate (e.g. Heger & Woosley 2002; Heger et al. 2003; Langer et al. 2007; Takahashi et al. 2015; Spera & Mapelli 2017; Woosley 2017; Marchant et al. 2019; Iorio et al. 2022; Tanikawa et al. 2023). Moreover, detailed stellar evolution calculations show that the PISN range tends to shift to higher $M_{\rm ZAMS}$ at increasing metallicity (e.g. Heger & Woosley 2002; Heger et al. 2003; Spera & Mapelli 2017).

Since PISNe are expected to occur only in low-metallicity stars, pristine, very-low-metallicity Population III stars (Pop III) have been traditionally considered as main PISN progenitors (e.g. El Eid, Fricke & Ober 1983; Ober, El Eid & Fricke 1983; Baraffe, Heger & Woosley 2001; Umeda & Nomoto 2001; Heger & Woosley 2002; Scannapieco et al. 2005; Wise & Abel 2005; Langer et al. 2007; Kasen et al. 2011; Dessart et al. 2012; Pan, Kasen & Loeb 2012; Yoon, Dierks & Langer 2012; Whalen et al. 2013; de Souza et al. 2013, 2014; Whalen et al. 2014; Smidt et al. 2015; Magg et al. 2016; Regős, Vinkó & Ziegler 2020; Venditti et al. 2024; Bovill et al. 2024; Wiggins et al. 2024). However, the fact that stellar evolution simulations allow for PISNe up to $\sim 0.5\,Z_{\odot}$, suggests that also higher Z, Population II/I (Pop II/I) stars might give a significant contribution to the PISN rate.

Comprehending the physics behind and the occurrence of PISNe, particularly in relation to their surrounding environments, holds a myriad of astrophysical implications.

For instance, the study of PISNe is strongly linked to the debate on the upper limit of the stellar initial mass function (IMF). Stars with masses consistent with $\gtrsim 200 - 300\,{\rm M}_{\odot}$ have indeed been observed in local galaxies (Crowther et al. 2010, 2016; Evans et al. 2010; Walborn et al. 2014; Schneider et al. 2018; Crowther 2019; Bestenlehner et al. 2020; Brands et al. 2022; Kalari et al. 2022), challenging the previous consensus that placed the maximum stellar mass at $\sim$150 $\rm M_{\odot}$ (Vink 2015). The existence of VMSs is also supported by chemical abundances studies (e.g. Romano et al. 2017, 2020a, b; Goswami et al. 2021, 2022). The observation of massive stellar BH binaries in gravitational waves (GWs) offers a new opportunity to investigate VMSs, even though all confident detections achieved so far do not necessarily require such massive progenitors (e.g. Spera, Mapelli & Bressan 2015; Abbot et al. 2016, 2020; Spera & Mapelli 2017; Vink et al. 2021). Due to the very high masses of PISN progenitors, the location of the IMF upper limit can critically determine the PISN rate.

Moreover, PISNe can help to shed light on many uncertain aspects of galaxy evolution. Indeed, PISN occurrence strongly depends on the properties of the galactic environments in which they take place. Therefore, their study requires a determination of the Z-dependent star formation rate density (SFRD) across cosmic history. This quantity defines the amount of mass available to form stars in the Universe, per unit time, comoving volume, and metallicity. To estimate it, two main approaches are usually adopted, relying either on cosmological simulations (e.g. O'Shaughnessy et al. 2016; Mapelli et al. 2017; Lamberts et al. 2018; Mapelli & Giacobbo 2018; Artale et al. 2019), or on empirical prescriptions for the SFRD and galaxy metallicity distribution, derived from observations (e.g. Lamberts et al. 2016; Belczynski et al. 2016a; Cao, Lu & Zhao 2017; Elbert, Bullock & Kaplinghat 2017; Li et al. 2018; Boco et al. 2019; Chruslinska & Nelemans 2019; Neijssel et al. 2019; Boco et al. 2021; Santoliquido et al. 2021). Many uncertainties still exist around this subject (see e.g. Chruslinska & Nelemans 2019; Neijssel et al. 2019; Boco et al. 2021; Santoliquido et al. 2021 for a comprehensive overview). In particular, the metallicity distribution of galaxies is still considerably unknown. Moreover, the low-mass end of the galaxy stellar mass functions (GSMFs), describing the mass distribution of galaxies, is still poorly constrained, since low-mass galaxies are very faint and thus difficult to observe. Specifically, it is not clear whether the GSMF slope in this mass range is constant, or redshift dependent (see e.g. Navarro-Carrera et al. 2024, where the latter case is supported by *JWST* data at redshifts $4 \lesssim z \lesssim 8$).

PISNe are also commonly invoked in studies about the chemical enrichment of the Universe (e.g. Ricotti & Ostriker 2004; Matteucci & Pipino 2005; Ballero, Matteucci & Chiappini 2006; Cherchneff & Dwek 2009; Rollinde et al. 2009; Cherchneff & Dwek 2010), and in particular to explain the chemical abundance patterns observed in the Milky Way and local galaxies (e.g. Goswami et al. 2021; Kojima et al. 2021; Goswami et al. 2022). The detection of PISN descendants, that is, stars with chemical abundances compatible with at least partial enrichment by a PISN, represents another avenue to find out about PISN occurrence, besides direct observation (e.g. Heger & Woosley 2002; Aoki et al. 2014; Takahashi, Yoshida & Umeda 2018; Salvadori et al. 2019; Caffau et al. 2022; Aguado et al. 2023; Koutsouridou, Salvadori & Ása Skúladóttir 2023; Xing et al. 2023). Hence, obtaining insights into the existence and rate of PISNe across cosmic time would have strong implications for numerous unresolved inquiries in both astrophysics and cosmology.

In this work, we compute the PISN rate as a function of redshift, by combining up-to-date stellar evolution tracks from the PARSEC and FRANEC codes, with an up-to-date semi-empirical determination of the Z-dependent SFRD across cosmic history. The aim is to study the dependence of the PISN rate on stellar and galactic prescriptions, an aspect which has not been explored extensively in the past. We also compute the ratio between PISN and CCSN rate, in order to provide

a comparison with these observed transients. Finally, we explore the properties of the favourable PISN host galaxies. This work represents the premise to a follow-up work, where we will employ the theoretical framework presented here to study PISN observability with the *JWST*, and address the question why these transients have never been observed. These works offer the opportunity to put constraints on stellar and galaxy evolution models, via the comparison with possible future PISN observations, or with the absence of observations in the eventuality that they are never discovered.

The paper is structured as follows. In Section 2, we present our theoretical framework. We start by describing our semi-empirical, Z-dependent SFRD determination, and how we use stellar evolution tracks to compute the number of PISNe produced per unit star-forming mass. We also show the considered variations on stellar and galactic prescriptions, and how we finally compute the PISN rate. Our results are presented in Section 3, and discussed in Section 4, where we also show additional variations. We draw our conclusions in Section 5.

Throughout this work, we assume the flat lambda-cold dark matter cosmology from Planck Collaboration VI (2020), with parameters $\Omega_M = 0.32$, $\Omega_b = 0.05$, and $H_0 = 67\ \mathrm{km\ s^{-1}\ Mpc^{-1}}$. A standard Kroupa IMF is adopted (Kroupa 2001), defined from 0.1 $M_\odot$. The IMF upper limit is among the parameters we decide to vary. Following Caffau et al. 2010, we use the value of $Z_\odot = 0.0153$ for the Solar metallicity, and $12 + \log(\mathrm{O/H})_\odot = 8.76$ for the Solar oxygen abundance.

2 METHODS

We take into account how galaxies evolve throughout cosmic history by constructing a detailed semi-empirical determination of the Z-dependent SFRD, $\mathrm{d}^3 M_{\rm SFR}/\mathrm{d}t\mathrm{d}V\mathrm{d}\log Z$, directly based on observations, following Boco et al. (2021). This provides us with the amount of mass available for star formation at a certain redshift, per unit time, comoving volume, and metallicity. In order to compute the number of PISNe produced per unit star-forming mass, $\mathrm{d}N_{\rm PISN}/\mathrm{d}M_{\rm SFR}$, we make use of stellar evolution tracks computed with the PARSEC code (Bressan et al. 2012; Chen et al. 2014, 2015; Tang et al. 2014; Costa et al. 2019, 2021; Nguyen et al. 2022). Finally, we compute the PISN rate density as a function of redshift by convolving these two quantities, according to the following formula:

$$\frac{\mathrm{d}^2 N_{\rm PISN}}{\mathrm{d}t\mathrm{d}V}(z) = \int \mathrm{d}\log Z\ \frac{\mathrm{d}^3 M_{\rm SFR}}{\mathrm{d}t\mathrm{d}V\mathrm{d}\log Z}(Z, z) \times \frac{\mathrm{d}N_{\rm PISN}}{\mathrm{d}M_{\rm SFR}}(Z). \quad (1)$$

We describe in detail how we compute each of these quantities in the following sections. In order to account for the uncertainties in stellar and galaxy evolution models, we decide to follow a variational approach, considering alternative stellar evolution codes, and different values for the relevant stellar and galactic parameters.

2.1 Galaxy evolution

We follow the semi-empirical approach presented in Boco et al. (2021) in order to compute the Z-dependent SFRD, with some updates informed by more recent works (Chruślińska et al. 2021; Popesso et al. 2022). This approach is built on galaxy observations up to $z = 6$. First, we compute galaxy SMFs, providing a galaxy statistics based on their stellar mass, $\Phi(M_\star) = \mathrm{d}^2 N/\mathrm{d}V\mathrm{d}\log M_\star$. Here, N indicates the number of galaxies, $M_\star$ their stellar mass, and V the comoving volume. We then convolve the SMFs with the galaxy main sequence (MS), $\psi(M_\star)$, relating the galaxy stellar mass to their SFR, ψ. We also implement a distribution of galaxies as a function of SFR, $\mathrm{d}p/\mathrm{d}\log\psi$, as indicated by observations (see below). In this way we are able to obtain SFR functions (SFRFs), that is, a galaxy statistics based on SFR. For the galaxy metallicity, we define a lognormal distribution, $\mathrm{d}p/\mathrm{d}\log Z\,(Z, Z_{\rm FMR})$, with a constant dispersion σ_Z. The mean value, $Z_{\rm FMR}$, is given by the fundamental metallicity relation (FMR) linking galaxy mass, metallicity, and SFR. We finally convolve all these factors according to the following formula, where we integrate over $M_\star$ and ψ:

$$\begin{aligned}\frac{\mathrm{d}^3 M_{\rm SFR}}{\mathrm{d}t\mathrm{d}V\mathrm{d}\log Z}(Z, z) = &\int \mathrm{d}\log M_\star \frac{\mathrm{d}^2 N}{\mathrm{d}V\mathrm{d}\log M_\star}(M_\star, z) \\ &\times \int \mathrm{d}\log\psi\ \psi \frac{\mathrm{d}p}{\mathrm{d}\log\psi}(\psi, M_\star, z) \\ &\times \frac{\mathrm{d}p}{\mathrm{d}\log Z}(Z, Z_{\rm FMR}(M_\star, \psi)). \quad (2)\end{aligned}$$

Each ingredient in equation (2) is computed as described in the following.

2.1.1. *SMF + MS*

We follow the work by Chruslinska & Nelemans (2019) in order to compute the galactic SMFs. They perform a comprehensive determination by gathering several previous results from the literature, consisting in Schechter and/or double Schechter analytical fits to observational data. In particular, they consider discrete redshift bins, and in each of them they average among previous results in order to obtain the SMFs at the corresponding redshifts. The SMFs at arbitrary redshifts are computed by interpolating between these curves. In order to take into account the uncertainties around the low-mass end of the SMFs, they consider two variations, defining a constant low-mass end slope, $\alpha_{\rm SMF} = -1.45$, or prescribing a redshift dependence, $\alpha_{\rm SMF}(z) = -0.1z - 1.34$. In Fig. 1, we show the SMFs we obtain

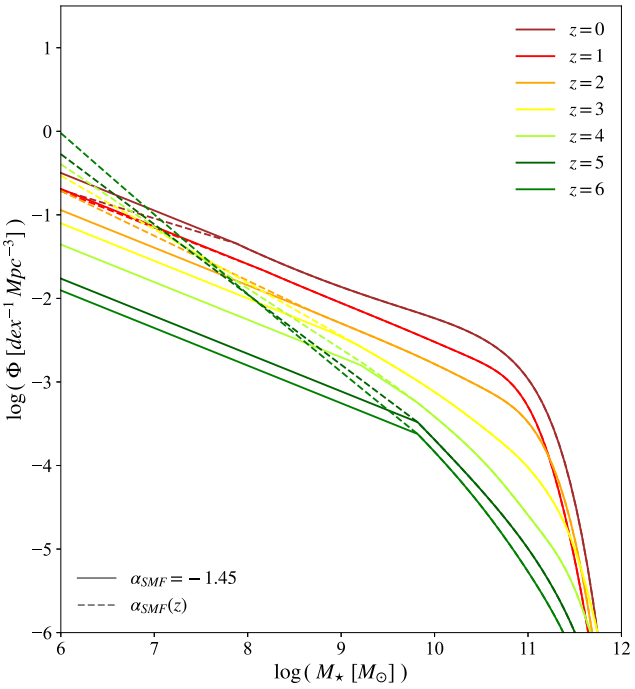

Figure 1. SMFs computed following Chruslinska & Nelemans (2019),at redshift $z = 0$ to 6. We show both variations with $\alpha_{\rm SMF} = -1.45$ and $\alpha_{\rm SMF}(z) = -0.1z - 1.34$, in solid and dashed lines, respectively.

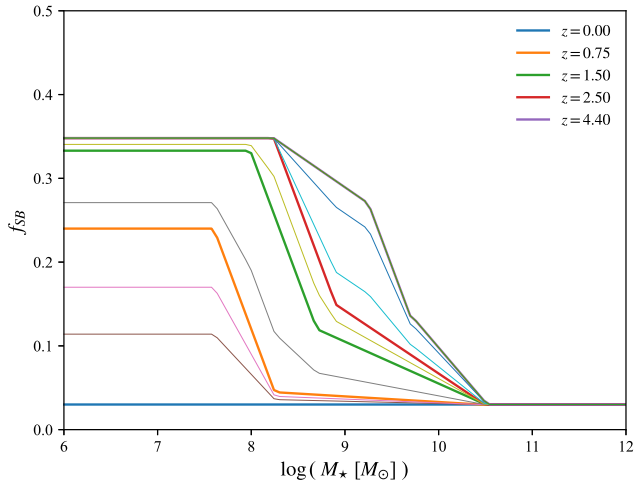

Figure 2. SB fractions $f_{\rm SB}$ as a function of $M_\star$, for different z, computed following Chruślińska et al. (2021). Thicker lines represent the $f_{\rm SB}$ computed for five initial redshifts (shown in the legend), while the $f_{\rm SB}$ at intermediate redshifts are computed by interpolation. At $z = 0$, $f_{\rm SB}$ remains constant at 0.03, while above $z = 4.4$ all curves saturate at 0.35, due to the dearth of observational data at those high redshifts.

by following the same procedure, for both $\alpha_{\rm SMF}$ cases (solid and dashed lines, respectively), in the redshift range relevant to this work, $0 \leq z \leq 6$.

It is to be noted that Chruslinska & Nelemans (2019) adopt a Kroupa IMF up to 100 $M_\odot$, while we extend it up to 300 $M_\odot$, as we will see later. This should not affect our results significantly, given that the Kroupa IMF predicts a relatively low number of massive stars between 100 and 300 $M_\odot$. Therefore the SMFs are not expected to differ appreciably.

We define our galactic MS following Popesso et al. (2022), which is the most complete determination up to date, taking into account all previous works in the literature and covering an unprecedented redshift and mass range, $0 < z < 6$ and $10^{8.5}$–$10^{11.5} M_\odot$. Additionally, we implement a double-Gaussian distribution in SFR, following Sargent et al. 2012:

$$\frac{{\rm d}p}{{\rm d}\log\psi}(\psi, M_\star, z) = \frac{f_{\rm MS}}{\sigma_{\rm MS}\sqrt{2\pi}} \exp\left[-\frac{(\log\psi - \langle\log\psi\rangle_{\rm MS})^2}{2\sigma_{\rm MS}^2}\right] + \\ + \frac{f_{\rm SB}}{\sigma_{\rm SB}\sqrt{2\pi}} \exp\left[-\frac{(\log\psi - \langle\log\psi\rangle_{\rm SB})^2}{2\sigma_{\rm SB}^2}\right], \tag{3}$$

where $\langle\log\psi\rangle_{\rm MS}$ is the MS relation, and $\sigma_{\rm MS} = 0.188$. As one can note by looking at the second term, we also consider the presence of starbursts (SBs), that is, galaxies experiencing intense star formation, located in a separate region above the MS in the $\psi - M_\star$ plane. The mean of the SB distribution is given by $\langle\log\psi\rangle_{\rm SB} = \langle\log\psi\rangle_{\rm MS} + 0.59$, while $\sigma_{\rm SB} = 0.243$. $f_{\rm MS}$ and $f_{\rm SB}$ are the fractions of MS and SB galaxies, respectively, such that $f_{\rm MS} + f_{\rm SB} = 1$. Differently from Boco et al. (2021), where a fixed SB fraction $f_{\rm SB} = 0.03$ is assumed, we implement a dependence of $f_{\rm SB}$ on galaxy stellar mass and redshift, as done in Chruślińska et al. (2021). In Fig. 2, we show the $f_{\rm SB}$ we compute following their work. This prescription enhances $f_{\rm SB}$ at low masses and increasing redshifts, bringing it from 0.03 up to 0.35. After $z = 4.4$, $f_{\rm SB}$ saturates at values constant in z. All in all, the $M_\star$ and z dependencies enter in equation (3) through $\langle\log\psi\rangle_{\rm MS}$, $\langle\log\psi\rangle_{\rm SB}$, $f_{\rm MS}$, and $f_{\rm SB}$.

2.1.2. Z distribution

The FMR prescribes a correlation between galaxy stellar mass, SFR, and metallicity, $Z_{\rm FMR}(M_\star, \psi)$. We define it following Curti et al. 2020:

$$Z_{\rm FMR}(M_\star, \psi) = 8.779 - (0.31/2.1) \times \log\left(1 + (M_\star/M_0(\psi))^{-2.1}\right), \tag{4}$$

where $M_0(\psi) = 10^{10.11} \times \psi^{0.56}$.

Furthermore, we assume Z to follow a log-normal distribution around the FMR,

$$\frac{{\rm d}p}{{\rm d}\log Z}(Z, Z_{\rm FMR}(M_\star, \psi)) \propto \exp\left[-\frac{(\log Z - \log Z_{\rm FMR}(M_\star, \psi))^2}{2\sigma_Z^2}\right], \tag{5}$$

We consider variations $\sigma_Z = [0.15, 0.35, 0.70]$, to study the effect of this parameter on the PISN rate.

We report the final outcome of our galactic model in Fig. 3, where we show the Z-dependent SFRD for all three variations on σ_Z, fixing $\alpha_{\rm SMF} = -1.45$ (equation 2). We also show the metallicity corresponding to the SFRD peak, as a function of redshift, for both variations on $\alpha_{\rm SMF}$ (solid and dashed white lines), as well as the position of the overall SFRD peak (white star). In Fig. 4, we instead report the SFRD as a function of redshift, obtained by integrating the previous quantity over Z, according to:

$$\frac{{\rm d}^2 M_{\rm SFR}}{{\rm d}t{\rm d}V}(z) = \int {\rm d}\log Z \frac{{\rm d}^3 M_{\rm SFR}}{{\rm d}t{\rm d}V{\rm d}\log Z}(Z, z). \tag{6}$$

In order to show the agreement of our SFRD with observations, we also plot several empirical determinations from galaxy surveys in different bands (Schiminovich et al. 2005; Gruppioni et al. 2013, 2020; Dunlop et al. 2016; Rowan-Robinson et al. 2016; Novak et al. 2017; Casey et al. 2018; Liu et al. 2018; Bouwens et al. 2021), as well as the Kistler et al. (2009) and Kistler, Yuksel & Hopkins (2013) data obtained from long gamma-ray burst observations.

Different ways to compute this quantity exist in the literature. Among empirical or semi-empirical approaches, one of the main alternatives is to rely on SFRFs, describing the number density of galaxies with a given SFR. They can be computed from galaxy ultraviolet and infrared luminosity functions, using the conversion between luminosity and SFR. Moreover, it is possible to implement a Z-dependence on the SFRD using a mass–metallicity relation, linking galaxy mass and metallicity, instead of a FMR. Another common approach is to combine an existing SFRD determination with a standalone galaxy Z distribution in redshift. We refer to Boco et al. (2021) for a comparison between these different methods. Finally, we stress that one of the main advantages of empirical determinations like ours, with respect to those relying on cosmological simulations, is that they are free from theoretical assumptions, being directly informed by observations.

2.2 Stellar evolution

The second part of our method consists in computing the number of PISNe produced per unit star-forming mass available, ${\rm d}N_{\rm PISN}/{\rm d}M_{\rm SFR}$. We do so by integrating an assumed IMF, $\phi(M)$, over the mass range of PISN progenitors, according to the following formula:

$$\frac{{\rm d}N_{\rm PISN}}{{\rm d}M_{\rm SFR}}(Z) = \frac{\int_{M_{\rm entry}}^{M_{\rm exit}} \phi(M){\rm d}M}{\int_{0.1}^{M_{\rm up}} M\phi(M){\rm d}M}, \tag{7}$$

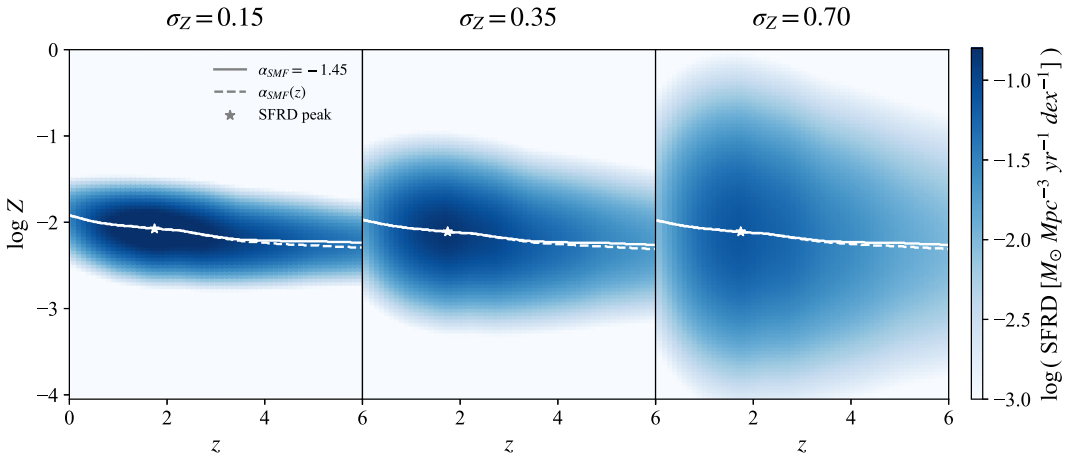

Figure 3. SFRD as a function of redshift and metallicity, for $\sigma_Z = [0.15, 0.35, 0.70]$ (from left to right), and $\alpha_{SMF} = -1.45$. The colour bar shows the SFRD values. Solid (dashed) lines indicate the metallicity at which the SFRD peaks as a function of redshift, for $\alpha_{SMF} = -1.45$ ($\alpha_{SMF} = \alpha_{SMF}(z)$). Stars indicate the redshift corresponding to the SFRD peak.

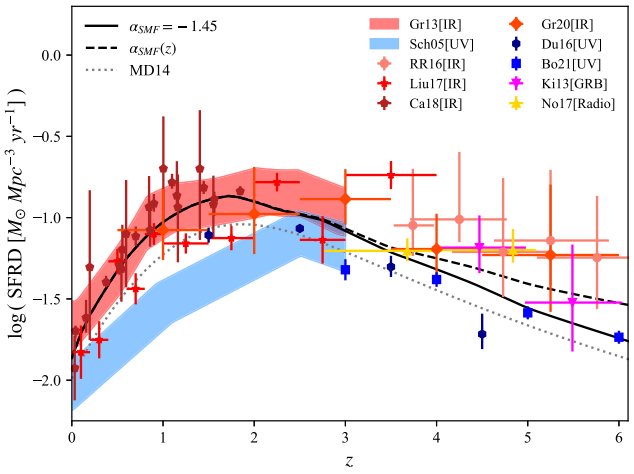

Figure 4. Cosmic SFR density as a function of redshift, for $\alpha_{SMF} = -1.45$ and $\alpha_{SMF}(z)$ variations (solid and dashed black lines respectively). The data points and bands show the observational determinations available at different redshifts, obtained from galaxy surveys in different bands (see the text for references). We also show the Madau & Dickinson (2014) plot, corrected for our Kroupa IMF, for comparison (dotted grey line).

where M_{entry} and M_{exit} are the ZAMS masses for entering and exiting the PISN range, respectively. We adopt a Kroupa IMF (Kroupa 2001) defined in the mass range $[0.1 - M_{up}]$ $M_\odot$, where the lower limit is the minimum stellar mass to ignite core H burning. We choose to vary M_{up} from 150 to 300 $M_\odot$, in order to study the effects of different IMF upper limits on the PISN rate (see Appendix B for an additional variation with $M_{up} = 600$ $M_\odot$).

In order to compute M_{entry} and M_{exit}, we adopt the criterion on the final core mass, according to which a star will develop pair instability leading to a PISN explosion if its He or CO core mass ($M_{He/CO}$) in the pre-SN stage lies in a certain range. Then we employ stellar evolution tracks to link the initial, ZAMS mass to the final core mass, and obtain a M_{ZAMS} range for PISN progenitors. We gather several works studying the evolution of VMSs from the literature, where the authors consider a range of He and/or CO core masses for which stars end their life as PISN (Heger & Woosley 2002; Heger et al. 2003; Langer et al. 2007; Chatzopoulos & Wheeler 2012; Takahashi et al. 2015; Spera, Giacobbo & Mapelli 2016; Belczynski et al. 2016b; Spera & Mapelli 2017; Woosley 2017; Eldridge, Stanway & Tang 2018; Farmer et al. 2019; Marchant et al. 2019; Stevenson et al. 2019; Belczynski 2020; du Buisson et al. 2020; Kinugawa, Nakamura & Nakano 2020; Marchant & Moriya 2020; Tanikawa et al. 2021; Woosley & Heger 2021; Briel et al. 2022; Olejak et al. 2022; Briel, Stevance & Eldridge 2023; Tanikawa et al. 2023). Specifically, we decide to adopt the criterion on M_{CO}, instead of M_{He}, motivated by the fact that it is in the CO core that PI sets in. Moreover, varying C burning reaction rate, and consequently the C/O ratio at He core depletion, impacts significantly on the position of the star in the core density–temperature plane, that is, on the onset of PI (e.g. Farmer et al. 2019). In any case, as shown in Appendix A, varying between CO and He core criterion does not significantly affect our results. Due to the uncertainties existing on these ranges, we consider an optimistic and pessimistic variation, featuring the widest and shortest intervals based on the literature, that is, $M_{CO} \in [60 - 105]$ and $\in [45 - 120] M_\odot$, respectively. We also consider an intermediate case with $M_{CO} \in [55 - 110] M_\odot$.

We consider two sets of stellar evolution tracks computed with the PARSEC code, that follows the evolution of single stars from the pre-MS up to the most advanced burning phases. The first set (Bressan et al. 2012; Chen et al. 2014, 2015; Tang et al. 2014) was used in Spera & Mapelli (2017), implemented in the binary population synthesis code SEVN, and has been employed in several works in the last years. We will address it as PARSEC-I. The second and more recent set, which we will call PARSEC-II (Costa et al. 2019, 2021), was implemented in the recently published version of SEVN (Iorio et al. 2022).

In PARSEC-II, the nuclear reactions and elemental mixing are coupled and solved at the same time in a diffusive scheme (Marigo et al. 2013; Costa et al. 2019). Additionally, PARSEC-II has updated prescriptions for the mass loss of massive stars, including Wolf–Rayet (WR) type wind (Sander et al. 2019, see Costa et al. 2021 for more details). Moreover, these new models include an updated equation of state, also accounting for the effects of e–e^+ pair creation.

In order to see the effects of varying stellar evolution code, we also consider the results obtained with the FRANEC stellar evolution code (Chieffi & Limongi 2013; Limongi & Chieffi 2018). Comparing the results obtained using different sets of evolutionary tracks, especially

when they are calculated by different groups that use different codes, is not a trivial procedure because, besides differences already arising from the different numerical procedures adopted, there are also variations due to different assumptions in the model calculations, and even in the description of physical complex phenomena that still require a calibration against observations. For example, different assumptions could refer to the criterion (basically Schwarzschild or Ledoux) adopted to establish whether a region is stable or not to convective motions. Instead, the calibration process may refer to the calibration against the Solar model to fix the value of the mixing length theory, or to the size of the overshooting adopted in the convective core or at the bottom of the convective envelope. It will be impossible to trace back all these differences (and their impact on the results), and we will list below only the major differences that we believe must be considered when performing a sound comparison, leaving the details to the individual papers that describe the model calculations.

PARSEC models use the Caffau et al. (2010) solar partition of heavy elements (with $Z_\odot = 0.0153$), even at very low metallicity, while FRANEC adopts the Asplund et al. (2009) solar partition (with $Z_\odot = 0.0134$), and consider α-element enhancement at low metallicity (see e.g. Limongi & Chieffi 2018). This small discrepancy can cause models to evolve at slightly different luminosities already on the MS (Sibony et al. 2024). Furthermore, since the metallicity of the Sun is used as a reference in the scaling law of the mass-loss process with metallicity, this small difference can induce differences in the mass-loss rates at different absolute metallicities, even adopting the same mass-loss prescriptions.

PARSEC-I provides tracks for 12 different metallicities from 1×10^{-4} to 3×10^{-2}, while PARSEC-II considers 13 metallicities from 1×10^{-4} to 4×10^{-2}. The FRANEC tracks are instead available for four metallicities, from 3×10^{-5} to $\sim 1.35 \times 10^{-2}$. We linearly interpolate to obtain stellar tracks at metallicities in between, following Iorio et al. (2022). Moreover, while the PARSEC-II tracks are computed for masses up to 600 $M_\odot$, the PARSEC-I and FRANEC ones extend up to $\gtrsim$300 and 120 $M_\odot$, respectively. We linearly extrapolate at higher masses. We caution that the actual trend of the stellar tracks at these high masses might deviate quite significantly from this approximation, which should be taken into account in examining our results.

For the convective stability, PARSEC models adopt the Schwarzschild criterion, while FRANEC models adopt the Ledoux one. The latter is more restrictive than the former and, if we consider that the core overshooting prescriptions are slightly different between PARSEC and FRANEC, and that PARSEC also accounts for overshooting from the bottom of the convective envelope, it is clear the the evolution in the low-mass range of massive stars may be different (but given the high non-linearity of the solutions, it is not easy to trace back the nature of the differences).

On the other hand, the evolution of more massive stars is strongly regulated by mass loss (Smith 2014), and the effect that may have the strongest impact on the results is the adopted prescription for the mass-loss rates in the different evolutionary phases. Concerning massive stars, we remind that PARSEC includes radiative winds depending on the mass and evolutionary phase as described in Chen et al. (2015) and Costa et al. (2021). In particular, in hot stars ($T_{\rm eff} \geq 10\,000$ K), it uses the mass-loss prescriptions by Vink, de Koter & Lamers (2000, 2001), including a surface iron abundance dependence; it also includes a dependence on the Eddington ratio (Grafener & Hamann 2008; Vink et al. 2011), which becomes important for the most luminous stars. For WR stars, that is, when $T_{\rm eff} \geq 20\,000$ K and the hydrogen surface abundance is less than 0.3 in mass fraction, PARSEC-II uses the luminosity-dependent prescription for the mass loss from Sander et al. (2019),while PARSEC-I uses a combination of literature mass-loss rates. Finally both PARSEC-I and II use the prescription by de Jager, Nieuwenhuijzen & van der Hucht (1988) for cold massive stars (i.e. red super giants, RSGs).

In FRANEC models, the Eddington ratio is checked within each structure, and if a region where it is larger than unity is found, this region and the overlying layers are removed from the star. Furthermore, for RSGs a dust-driven mass-loss rate is used (van Loon et al. 2005). Both of these latter recipes for the mass-loss rates may cause strong differences in the evolution of the most massive stars, even for those with initial mass as low as $M_{\rm ZAMS} = 15$ or 20 $M_\odot$ at near-solar metallicity.

All stellar tracks employed here are calculated without rotation. The main effects of including rotation would be increased mass loss, and bigger cores due to enhanced chemical mixing. Overall, we expect the $M_{\rm ZAMS}$ ranges of PISN progenitors to shift to lower masses (see also the recent work by Winch et al. 2024), resulting in higher PISN rates. It would be interesting to evaluate the entity of these effects by employing evolution tracks of rotating stars, which we do not explore here.

It is important to note that, as one can see, in this work we restrict to metallicities down to 10^{-4}, and redshifts up to $z = 6$, effectively only considering Pop II/I stars as PISN progenitors. This is motivated by the fact that huge uncertainties still exist around quantities such as the SFRD at very high redshifts, $z > 6$, and the Pop III IMF, which prevents from extending the study to Pop III stars in a comparably robust way. We discuss this issue in more depth in Section 4.6.

Table 1 shows the $M_{\rm ZAMS}$ ranges obtained with each stellar evolution code, at some representative metallicities. We note that $M_{\rm up}$ cuts these ranges above its value. Masses greater than 300 $M_\odot$ were fixed to 300 $M_\odot$, since we only consider IMFs up to this value in this work (but see also Appendix B). As one can see, these ranges can differ quite significantly from the canonical $[140 - 260]$ $M_\odot$. Moreover, they generally shift to higher masses at higher metallicities. Indeed, mass loss due to stellar winds is enhanced, thus the star must be initially more massive in order to produce a core satisfying the PISN criterion. Above a certain metallicity, which depends on the considered variation, the core cannot reach this mass threshold. We refer to the maximum metallicity for a star to explode as PISN, as $Z_{\rm max}$. As we will later show, $Z_{\rm max}$ turns out to be a crucial quantity in determining the PISN rate.

In Fig. 5, we report the $\mathrm{d}N_{\rm PISN}/\mathrm{d}M_{\rm SFR}(Z)$ obtained using each stellar code, combined with different variations on $M_{\rm CO}$ criterion and $M_{\rm up}$. To avoid redundancy, among the 18 cases that we compute, we decide to select six representative combinations, described in Table 2. *F* stands for our fiducial variation. *P* represents our pessimistic case, producing the smallest amount of PISNe, while *O* is our optimistic case. All variations in the middle are marked with an *M*. One can clearly see the $Z_{\rm max}$ resulting from each combination, as the metallicity at which $\mathrm{d}N_{\rm PISN}/\mathrm{d}M_{\rm SFR}(Z)$ vanishes. The exact values are reported in Table 2. The effects of combining different stellar codes, $M_{\rm CO}$ range and $M_{\rm up}$, can be boiled down to $Z_{\rm max}$, and secondly to the height of the $\mathrm{d}N_{\rm PISN}/\mathrm{d}M_{\rm SFR}$ curve. For this reason, when presenting our results in Section 3, every stellar variation will be represented by the corresponding $Z_{\rm max}$.

We note that some different combinations would lead to results superimposing to the ones we show, due to the degeneracy of the PISN rate on stellar prescriptions, but falling in any case between our *P* and *O* variations.

Table 1. M_{ZAMS} ranges of PISN progenitors, for representative metallicities, obtained with the PARSEC-I, PARSEC-II, and FRANEC stellar evolution tracks. The ranges at metallicities in between the original ones from the stellar tracks are obtained via interpolation, as described in the text. All values are in solar units. Blanks indicate cases with no PISN, at $Z > Z_{max}$. Masses $> 300\,M_\odot$ are fixed to $300\,M_\odot$, that is, the highest M_{up} considered in this work (see Appendix B for an additional variation with $M_{up} = 600\,M_\odot$). The double intervals at $Z = 1 \times 10^{-4}$ of PARSEC-II are due to the non-monotonicity of the corresponding stellar track, which exits the PISN mass range and then re-enters again (see fig. 8 of Iorio et al. 2022).

M_{CO} \ Z	1×10^{-4}	1×10^{-3}	4×10^{-3}	8×10^{-3}	1×10^{-2}	2×10^{-2}
			PARSEC-I			
45–120	108–257	109–300	158–300	178–222	–	–
55–110	126–237	128–300	195–300	–	–	–
60–105	138–228	139–300	213–300	–	–	–
			PARSEC-II			
45–120	107–229	112–239	92–221	111–294	133–300	–
55–110	117–150 153–211	130–227	109–202	138–270	166–300	–
60–105	125–145 158–203	140–221	118–193	151–258	182–300	-
			FRANEC			
45–120	111–262	113–272	136–300	183–300	220–300	–
55–110	131–242	134–251	173–300	233–300	282–300	–
60–105	141–232	145–240	192–300	259–300	–	–

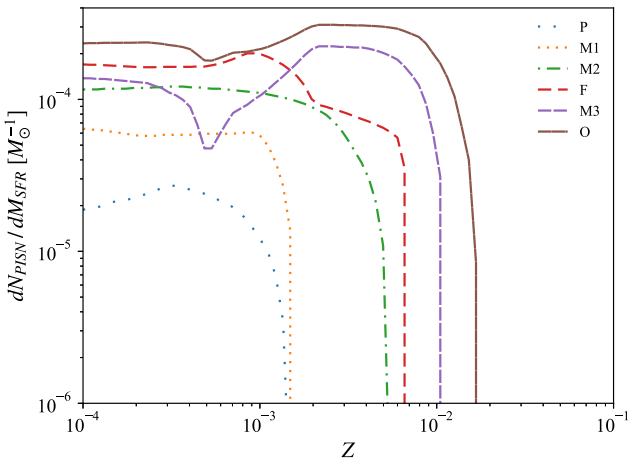

Figure 5. Number of PISN produced per unit star-forming mass as a function of metallicity, for different combinations of stellar evolution code, CO core mass criterion, and IMF upper limit (see Table 2). This figure clearly shows the maximum metallicity at which a star can explode as PISN, Z_{max}, according to each variation.

Table 2. Considered variations on stellar evolution code, CO core mass criterion, and IMF upper limit, as reference for Fig. 5. The maximum metallicity to have PISN according to each variation, Z_{max}, is also shown.

Name	Stellar code	$M_{CO}/M_\odot$	$M_{up}/M_\odot$	Z_{max}
P	FRANEC	60–105	150	1.5×10^{-3}
M1	PARSEC-I	55–110	150	1.5×10^{-3}
M2	FRANEC	45–120	150	5.5×10^{-3}
F	PARSEC-I	55–110	300	6.6×10^{-3}
M3	PARSEC-II	45–120	150	1.0×10^{-2}
O	PARSEC-II	45–120	300	1.7×10^{-2}

2.3 Rate computation

The galactic and stellar parts of our model provide us with the Z-dependent SFRD, $\mathrm{d}^3M_{SFR}/\mathrm{d}t\mathrm{d}V\mathrm{d}\log Z\,(Z,z)$, and the number of PISNe produced per unit star-forming mass, $\mathrm{d}N_{PISN}/\mathrm{d}M_{SFR}\,(Z)$, respectively. In order to finally compute the PISN event rate as a function of redshift, $\mathrm{d}^2N_{PISN}/\mathrm{d}t\mathrm{d}V\,(z)$, we need to convolve these two quantities by integrating over Z, as shown in equation (1).

In Section 3.4, we study the dependence of the PISN rate on galaxy stellar mass and metallicity, $M_\star$ and Z. In order to do that, we need to start from the SFRD defined also per unit $M_\star$, which we obtain by simply avoiding integrating over this quantity in equation (2). We then obtain the dependence on $M_\star$ and Z by integrating over z, after converting the unit volume into unit redshift via the comoving volume element per unit redshift and steradian, $\mathrm{d}V/\mathrm{d}z$:

$$\frac{\mathrm{d}^4M_{SFR}}{\mathrm{d}z\mathrm{d}t\mathrm{d}\log Z\mathrm{d}\log M_\star}(Z,M_\star,z) = \\ = \frac{\mathrm{d}^4M_{SFR}}{\mathrm{d}t\mathrm{d}V\mathrm{d}\log Z\mathrm{d}\log M_\star}(Z,M_\star,z)\times 4\pi\frac{\mathrm{d}V}{\mathrm{d}z}(z), \quad (8)$$

$$\frac{\mathrm{d}^3N_{PISN}}{\mathrm{d}t\mathrm{d}\log Z\mathrm{d}\log M_\star}(Z,M_\star) = \\ = \int \mathrm{d}z\,\frac{\mathrm{d}^4M_{SFR}}{\mathrm{d}z\mathrm{d}t\mathrm{d}\log Z\mathrm{d}\log M_\star}(Z,M_\star,z)\times\frac{\mathrm{d}N_{PISN}}{\mathrm{d}M_{SFR}}(Z). \quad (9)$$

By further integrating, one can get the PISN rate as a function of $M_\star$ or Z. The possibility to handle the masses of single galaxies represents one of the main advantages of SFRD semi-empirical determinations like the one employed in this work. In particular, here it allows us to identify the masses of the favourable PISN host galaxies, besides their metallicity, as we show in Section 3.4.

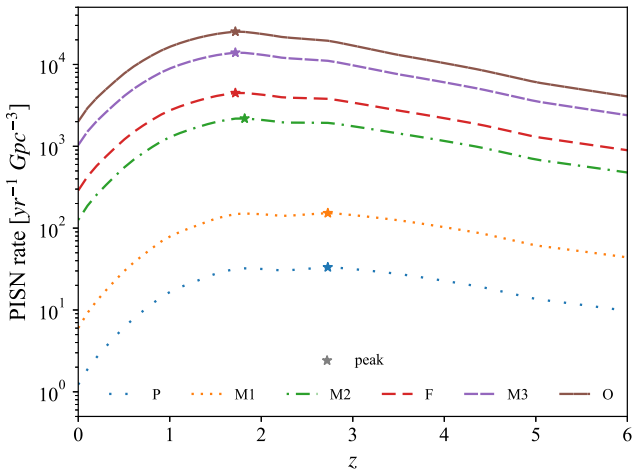

Figure 6. PISN rate as a function of z for our stellar variations on stellar evolution code, CO core mass criterion, and IMF upper limit. See Table 2 for a description of each variation. Stars indicate the peak of the PISN rate.

3 RESULTS

In the following section, we present the results obtained in this work. First, we show how our variations on stellar evolution code, CO core mass criterion and IMF upper limit, affect the PISN rate (Section 3.1). Then, we focus on the interplay between $Z_{\rm max}$, resulting from each stellar variation, and $\sigma_{\rm Z}$ in determining the PISN rate, and the effect of changing $\alpha_{\rm SMF}$ (Section 3.2). The aim is to study to what extent the uncertainties in both stellar and galactic models affect the PISN rate, and obtain a range of results spanning from a pessimistic to an optimistic case.

Differently from PISNe, several hundreds of CCSNe have been observed so far. Thus, it can be useful to compare the rates of these transients. We compute the ratio between PISN and CCSN rates, and show the results in Section 3.3, for all of our variations.

Finally, in Section 3.4, we study the dependence of the PISN rate on galaxy $M_\star$ and Z, in order to understand which galactic environments are favourable for PISN production, and how much galaxies with given properties contribute to the PISN rate.

3.1 Stellar variations

Fig. 6 shows the PISN rate density as a function of redshift, computed with equation (1) for the stellar variations described in Section 2.2. The parameters of the galactic model are fixed to $\sigma_{\rm Z} = 0.35$ and $\alpha_{\rm SMF} = -1.45$, which can be considered our fiducial values. The rate closely resembles the trend of the SFRD (Fig. 4), peaking at around $z = 2$ and smoothly declining towards higher redshifts.

We can see that our whole range of stellar variations, from pessimistic (P) to optimistic (O), leads to roughly three orders of magnitude in the PISN rate, with values at $z = 0$ from $\sim 10^0$ to $10^3 {\rm Gpc}^{-3}{\rm yr}^{-1}$, and values at peak from $\sim 3 \times 10^1$ to $2 \times 10^4 {\rm Gpc}^{-3}{\rm yr}^{-1}$. As can be easily understood, a larger $M_{\rm CO}$ interval produces larger $M_{\rm ZAMS}$ ranges for the progenitors, that is, more stars going into PISN. Analogously, extending the IMF from $M_{\rm up} = 150$ to $300\,{\rm M}_\odot$ adds the contribution from more massive stars. This translates into higher ${\rm d}N_{\rm PISN}/{\rm d}M_{\rm SFR}$, with increased $Z_{\rm max}$, allowing for the production of more PISNe, at higher metallicities (Fig. 5). As a result, one gets a higher PISN rate. For example, if we fix FRANEC as stellar evolution code and $M_{\rm up} = 150\,{\rm M}_\odot$, changing the $M_{\rm CO}$ criterion from $[60-105]$ to $[45-120]$ (i.e. variation P to $M2$) increases the rate by about two orders of magnitude. Selecting instead PARSEC-I, $M_{\rm CO} \in [55-110]$, and bringing $M_{\rm up}$ from 150 to $300\,{\rm M}_\odot$ ($M1$ to F), leads to between one and two orders of magnitude increase in the rate.

The effects described above are weaker going towards higher PISN rates. For example, if we consider PARSEC-II with $M_{\rm CO} \in [45-120]$, bringing $M_{\rm up}$ from 150 to $300\,{\rm M}_\odot$ ($M3$ to O) only leads to a factor ~ 2 difference in the rate. This can be understood by looking at Fig. 7, where we present the PISN rate distribution in the z–Z plane for variations P, F, and O (lower, middle, and upper panels, respectively). We decide to only select these variations for simplicity, being representative of the whole set. In particular, the central column shows results for $\sigma_{\rm Z} = 0.35$, considered here (other variations on $\sigma_{\rm Z}$ are discussed in the next section). These plots exhibit a sharp cut in the metallicity distribution, which is a direct effect of $Z_{\rm max}$, completely suppressing PISNe at higher metallicities. Variation O displays $Z_{\rm max} \gtrsim 10^{-2}$, thus including the majority of the contribution from the SFRD peak, located at metallicities just above or below 10^{-2} depending on redshift (see the white lines in Fig. 3). This can be best appreciated in Fig. 7 by comparing the PISN rate distribution with the SFRD contour levels, indicated by violet dashed lines. Also variation $M3$ includes a fair portion of the SFRD peak contribution, with only a slightly smaller $Z_{\rm max}$. Together with the fact that ${\rm d}N_{\rm PISN}/{\rm d}M_{\rm SFR}$ changes just by a factor less than 2, this causes the rate to increase only by a relatively small amount going from $M3$ to O. On the contrary, the PISN rate distribution for the more pessimistic variations (P and $M1$) extends to metallicities far below the SFRD peak. As a consequence, moving to variations $M2$ and F adds a significant contribution to the PISN rate, from metallicities closer to the SFRD peak. This effect is further enhanced by the stronger increase in ${\rm d}N_{\rm PISN}/{\rm d}M_{\rm SFR}$, especially from P to $M2$, with respect to the more optimistic cases.

As indicated by the stars in Fig. 6, also the peak of the PISN rate distribution in redshift appears to shift with stellar variations, an effect which is enhanced when combining with galactic variations (see the following section). It is due to the fact that, on average, metallicity tends to decrease with redshift, according to our Z-evolution recipe. Variations with lower $Z_{\rm max}$ thus favour the contribution to the PISN rate coming from high redshift. As a result, the position of the peak tends to shift towards higher redshifts, always below $z = 3$ considering only stellar variations.

3.2 Galactic variations

After showing how different stellar evolution prescriptions, and IMF upper limits, influence the PISN rate, we now focus on the variations on parameters $\sigma_{\rm Z}$ and $\alpha_{\rm SMF}$ of our galactic model (see Section 2.1).

As anticipated above, we find a strong interplay between $Z_{\rm max}$, resulting from the combination of stellar evolution code, $M_{\rm CO}$ criterion and $M_{\rm up}$, and $\sigma_{\rm Z}$. Among the stellar variations discussed in the previous section, for clarity we decide to select only the most pessimistic and optimistic cases (P and O), as well as the fiducial one (F). Fig. 8 shows the PISN rates we obtain for the combination of each of these variations, described by the corresponding $Z_{\rm max}$ (see Table 2), with different $\sigma_{\rm Z}$. As we can see, this results in PISN rates spanning roughly seven orders of magnitude considering values at $z = 0$, or five orders of magnitude considering values at $z = 6$. Most of this range is due to variations with lowest $Z_{\rm max} = 1.5 \times 10^{-3}$. Indeed, as already discussed in the previous section and shown in Fig. 7, such low $Z_{\rm max}$ removes the main contribution to the PISN rate, coming from metallicities close to the SFRD peak. Selecting a low $\sigma_{\rm Z}$ means considering a SFRD which does not extend to the lowest

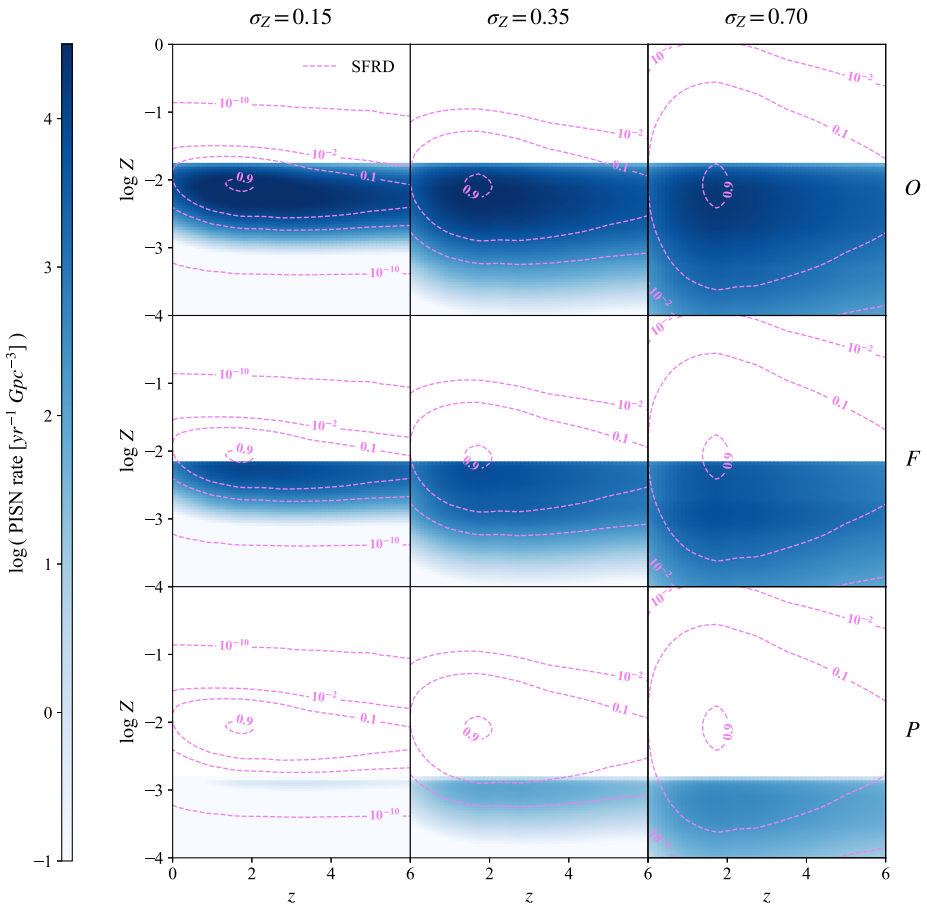

Figure 7. PISN rate as a function z and Z for variations P, F, and O on stellar evolution code, M_{CO} criterion, and M_{up} (lower, middle, and upper panels, respectively). See Table 2 for a description of each variation, and the corresponding Z_{max}. Different columns correspond to variations $\sigma_Z = 0.15$, 0.35, and 0.70 (left to right). We also show the SFRD contour levels for comparison (dashed lines), corresponding to fractions of 10^{-10}, 10^{-2}, 0.1, and 0.9 times its peak value.

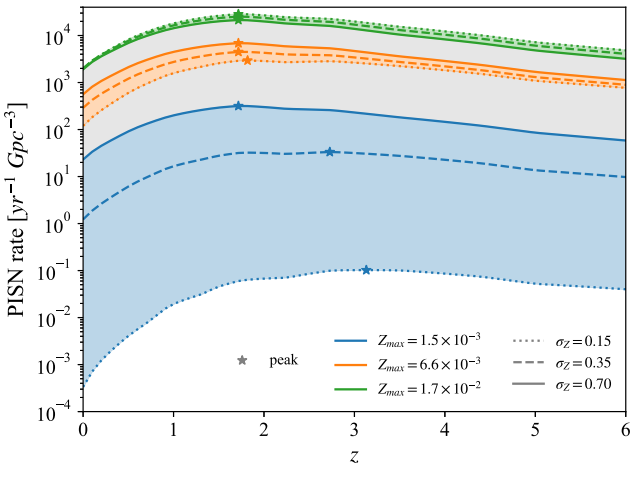

Figure 8. PISN rate as a function of z for different σ_Z, represented by different line styles, for Z_{max} corresponding to variations P, F, and O (see Table 2). Bands show the range of results produced by varying σ_Z, for every fixed Z_{max}. Stars indicate the peak of the PISN rate.

metallicities (Fig. 3, left panel), and as a consequence it strongly suppresses the PISN rate contribution from the tail of the galaxy metallicity distribution, $Z < Z_{max}$. This is the reason why variation P is so dependent on σ_Z. On the other hand, variation F yields a $Z_{max} = 6.6 \times 10^{-3}$ which is closer to the SFRD peak, and even in the lowest σ_Z case it includes part of that contribution (middle panels in Fig. 7). Therefore, the rate suffers less dramatically from changes in σ_Z. Variation O, with $Z_{max} = 1.7 \times 10^{-2}$ (top panels in Fig. 7), includes most of the contribution from the SFRD peak, making the dependence of the PISN rate on σ_Z even fainter. For all Z_{max}, this dependence appears more enhanced at lower redshifts. This is due to the fact that, as shown in Fig. 3, our SFRD experiences a substantial decrease below $z \sim 1$, resulting in a drop in the rate which is more and more significant going to lower σ_Z.

In variations P and F, the PISN rate increases with σ_Z. Indeed, in these cases Z_{max} lies below the peak of the SFRD, therefore a higher dispersion for the galaxy metallicity distribution increases the PISN rate below Z_{max}. On the contrary, variation O exhibits a rate increasing with decreasing σ_Z (namely, the dotted line is above the solid one). This is because in this case the peak of the SFRD is already included below Z_{max}. A higher σ_Z thus spreads a fraction of the PISN rate distribution above Z_{max}, where it gets lost (Fig. 7).

All in all, the PISN rate dependence on σ_Z varies dramatically with Z_{max}, increasing significantly going to lower values of this parameter (see the colour bands in Fig. 8, which get larger for lower Z_{max}). This shows the strong interplay between these parameters, which turns out to be crucial in determining the PISN rate. It is to be noted that, if we applied our galactic variations to the other

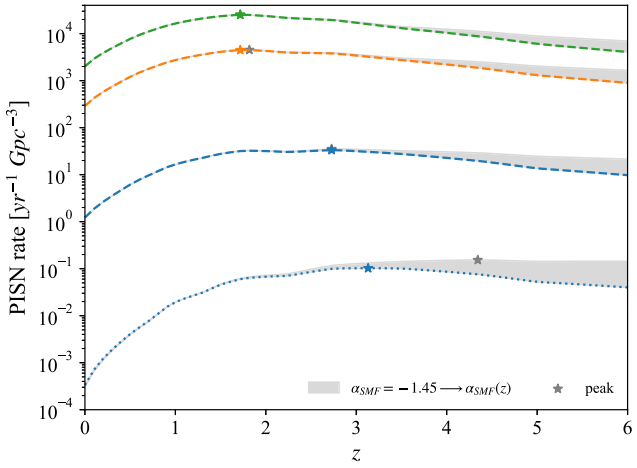

Figure 9. PISN rate as a function of z for $\alpha_{\rm SMF} = -1.45$ and $\alpha_{\rm SMF} = \alpha_{\rm SMF}(z)$ variations. We show the difference between the two variations with a band. Lines are as in Fig. 8 (note that we only reported some of those variations, for clarity). Stars indicate the peak of the PISN rate for each variation.

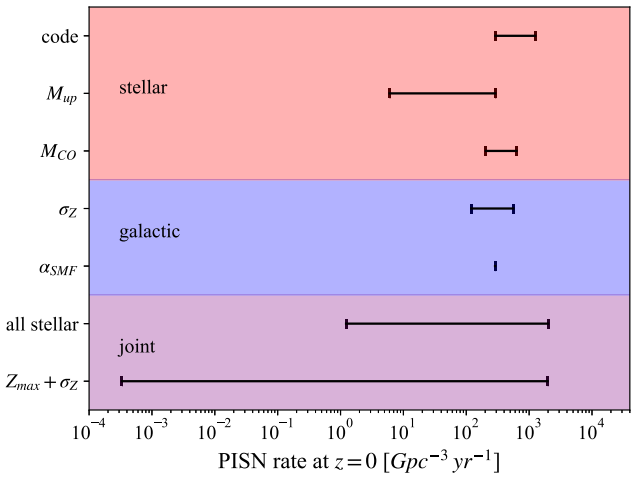

Figure 10. Uncertainties on the local PISN rate, computed at $z = 0$, due to each considered variation on stellar and galactic prescriptions (see the text). Global uncertainties due to all stellar variations combined are also shown, as well as those due to all possible combinations of $Z_{\rm max}$ and $\sigma_{\rm Z}$. Indeed, as highlighted in the text, the interplay between these two parameters plays a crucial role in determining the PISN rate. This figure was inspired by fig. 5 in Farmer et al. (2019).

stellar variations ($M1$, $M2$, and $M3$), we would obtain ranges of results partially superimposing to the ones we show for variations P, F, and O, as expressed by the grey band in Fig. 8. This reveals the degeneracy of the PISN rate on stellar and galactic prescriptions.

One can also notice a change in the peak position, from $z \sim 2$ (reproducing the SFRD peak) for $\sigma_{\rm Z} = 0.70$, to $z \gtrsim 3$ for $\sigma_{\rm Z} = 0.15$, in the lowest $Z_{\rm max} = 1.5 \times 10^{-3}$ variation. As explained in the previous section, this is an effect of the average metallicity decrease with redshift, prescribed by our Z evolution recipe. Here, this effect is enhanced by the $\sigma_{\rm Z} = 0.15$ variation, which further favours the PISN rate contribution from higher z.

Fig. 9 shows the effect of varying $\alpha_{\rm SMF}$ prescription. The grey band represents the difference between the constant $\alpha_{\rm SMF}$ case, $\alpha_{\rm SMF} = -1.45$, and that with $\alpha_{\rm SMF}$ defined as a function of redshift, $\alpha_{\rm SMF} = \alpha_{\rm SMF}(z)$. We consider only some of the variations reported in Fig. 8, for clarity purposes, since the trend is analogous. We can see that prescribing a redshift dependence for $\alpha_{\rm SMF}$ has an appreciable effect only at high redshifts, $z > 3 - 4$, where it increases the rate by a factor in any case smaller than one order of magnitude. Indeed, as shown in Fig. 1, this variation increases the number of galaxies at low masses, an effect which is stronger going to higher redshift. Moreover, the FMR prescribes that low-mass galaxies are also metal poor. Since this relation produces an average metallicity decreasing with redshift, these low-mass galaxies end up increasing the PISN rate at high redshift. This can also be appreciated by looking at Fig. 3, where one can see that the Z corresponding to the peak of the SFRD rate experiences a steeper decrease with redshift for variation $\alpha_{\rm SMF}(z)$, with respect to constant $\alpha_{\rm SMF}$ (an effect already shown in Chruslinska & Nelemans 2019). For the same reason, in variation P the peak of the $\alpha_{\rm SMF}(z)$ rate is shifted to between $z = 4$ and 5. Indeed, the effects of the $Z_{\rm max} - \sigma_{\rm Z}$ dependence are exacerbated, and in particular the PISN rate peak is brought to even higher redshifts than the constant-$\alpha_{\rm SMF}$ case.

We warn that the huge range we obtain for the PISN rate, by accounting for both stellar and galactic variations, is actually strongly dependent on the adopted Z-evolution prescriptions. We show this point in Section 4.5, where we explore an additional variation on FMR.

Finally, Fig. 10 shows the uncertainty intervals on the local PISN rate, computed at $z = 0$, due to each individual stellar and galactic variation (red and blue bands, respectively). Uncertainties due to all stellar variations, as well as all possible $Z_{\rm max} - \sigma_{\rm Z}$ combinations, are also shown (purple band). Every bar has been computed by fixing all other prescriptions to the fiducial case, and varying only the quantity of interest over the whole range. Notice how the $\alpha_{\rm SMF}$ variation does not lead to significant uncertainties on the PISN rate at $z = 0$ since, as explained in this section, it produces appreciable effects only at $z \sim 3 - 4$. This figure clearly shows how crucial the interplay between $Z_{\rm max}$ and $\sigma_{\rm Z}$ is in determining the PISN rate, extending the possible values downwards by several orders of magnitude, with respect to considering stellar and galactic variations separately.

3.3 PISN over CCSN ratio

In this section, we compute the ratio between the PISN and CCSN rate as a function of redshift. We follow the same procedure outlined in Section 2, fixing $\alpha_{\rm SMF} = -1.45$. We modify the mass range for IMF integration in equation (7) to [8–50] $M_\odot$. The upper ZAMS-mass limit of CCSN progenitors is highly uncertain, possibly ranging from $\sim 20 - 25$ to 125 $M_\odot$ (Heger & Woosley 2002; Heger et al. 2003; Dahlen et al. 2004, 2012; Cappellaro et al. 2005; Botticella et al. 2007, 2012; Smartt et al. 2009; Mattila et al. 2012; Melinder et al. 2012; Strolger et al. 2015; Petrushevska et al. 2016; Ziegler et al. 2022). For this reason, we select an intermediate, fiducial value of 50 $M_\odot$. We note that varying this value along the credible range does not change our results significantly, due to our bottom-heavy IMF. It is also to be stressed that, while for PISNe we obtain a dependence of the $M_{\rm ZAMS}$ range on metallicity, here we keep it constant, since the CCSN mass range is not expected to exhibit such a crucial dependence (namely CCSNe are expected to take place at all metallicities).

The results are shown in Table 3, for the same variations as Fig. 8. Analogously to the PISN rate, the PI/CC ratio spans from $\sim$ five to less than seven orders of magnitude, depending on redshift. It

Table 3. PISN over CCSN rate ratio for our set of $Z_{max} - \sigma_Z$ combinations (same as Fig. 8). We report values at $z = 0$ and 6, as well as the redshift at which the PISN rate peaks (z^{PI}_{peak}), in order to show the whole range across redshift.

σ_Z	PI/CC ($z = 0$)	PI/CC ($z = z^{PI}_{peak}$)	PI/CC ($z = 6$)
	Variation P ($Z_{max} = 1.5 \times 10^{-3}$)		
0.15	2.5×10^{-9}	1.4×10^{-7}	2.3×10^{-7}
0.35	9.2×10^{-6}	3.5×10^{-5}	5.5×10^{-5}
0.70	1.7×10^{-4}	2.4×10^{-4}	3.3×10^{-4}
	Variation F ($Z_{max} = 6.6 \times 10^{-3}$)		
0.15	9.2×10^{-4}	2.3×10^{-3}	4.5×10^{-3}
0.35	2.2×10^{-3}	3.5×10^{-3}	5.2×10^{-3}
0.70	4.3×10^{-3}	5.4×10^{-3}	6.6×10^{-3}
	Variation O ($Z_{max} = 1.7 \times 10^{-2}$)		
0.15	1.5×10^{-2}	2.2×10^{-2}	2.8×10^{-2}
0.35	1.5×10^{-2}	2.0×10^{-2}	2.4×10^{-2}
0.70	1.5×10^{-2}	1.7×10^{-2}	1.9×10^{-2}

ranges from 2.5×10^{-9} to 1.5×10^{-2} at $z = 0$, and from 2.3×10^{-7} to 2.8×10^{-2} at $z = 6$. Considering the redshift at which the PISN rate peaks for each variation, z^{PI}_{peak}, we get a PI/CC ratio ranging from 1.4×10^{-7} to 2.2×10^{-2}. The PISN rate dependence on $Z_{max} - \sigma_Z$ combinations is closely reproduced. This is easily understood, since the CCSN rate consists simply in the multiplication of the SFRD by the constant factor dN_{CCSN}/dM_{SFR}. Therefore, all the features of the PISN rate, which are ultimately due to its metallicity dependence, are again found in the PI/CC ratio. Values at $z = 6$ are always higher than at $z = 0$ and even z^{PI}_{peak}. This is because PISNe occur in environments with $Z < Z_{max}$, which are found preferentially at high redshift, according to our Z-evolution recipe. Since CCSNe are independent from metallicity, this favours PISNe over CCSNe, and causes their ratio to increase with redshift. The PISN rate drop at low redshifts, which is again due to the metallicity dependence and is thus absent in the CCSN rate, further accentuates this feature.

3.4 Host galaxy properties

In this section, we explore the dependencies of the PISN rate on galaxy mass and metallicity, and the interplay between them. Among our set of variations, we select three cases which best serve this purpose. The rates have been computed with equations (8) and 9, further integrating over $M_\star$ or Z. We stress that, due to the integration over z in equation (9), these rates represent the contribution coming from all redshifts up to $z = 6$.

In Fig. 11, we present a corner plot showing the individual and joint dependencies of the PISN rate on $M_\star$ and Z, for our fiducial stellar variation F, with galactic parameter $\sigma_Z = 0.15$. The difference between the two GSMF low-mass end slope cases, $\alpha_{SMF} = -1.45$ and $\alpha_{SMF} = \alpha_{SMF}(z)$, is indicated by a grey band. We find it informative to also show the SFR for the corresponding variations, with $\alpha_{SMF} = -1.45$, telling us about the total star-forming mass available in the first place. In particular, we show both the contour levels for the SFR as a function of $M_\star$ and Z, as well as the individual dependencies of the SFR on each of these quantities (violet dashed lines). We find again the sharp cut in the metallicity distribution due to Z_{max}, already discussed for Fig. 7. In this case $Z_{max} = 6.6 \times 10^{-3}$, which lies below the peak of the SFRD, as indicated by the violet dashed contours in the bottom left panel (see also Fig. 3). As a consequence, the main contribution to the PISN rate, coming from metallicities where the SFRD peaks, gets partially cut out. As discussed in Sections 3.1 and 3.2, this is the reason why the PISN rate turns out to be lower with respect to other variations with higher Z_{max}.

As one can see from the right panel of Fig. 11, the PISN rate peaks at metallicities just below Z_{max}, as a result of combining dN_{PISN}/dM_{SFR} (variation F in Fig. 5) with the SFRD. In other words, PISN production is favoured in low-Z environments, but stars formed at Z closer to the SFRD peak are more abundant, and therefore provide a larger contribution to the PISN rate.

In the top panel of Fig. 11, we show the PISN rate dependence on $M_\star$. This variation favours host galaxies with stellar masses between 10^9 and $10^{10} M_\odot$, from which comes the main contribution to the PISN rate. These masses are somewhat lower than those at which the SFR peaks, around $\sim 10^{10}$ $M_\odot$, as indicated by the violet dashed line in the top panel. Indeed, partially cutting the peak of the SFRD distribution over metallicity, also stops the rise of the PISN rate with $M_\star$, as can be clearly seen in the bottom left panel by comparing the PISN rate distribution with the SFR violet dashed contours. This is due to the correlation between $M_\star$ and Z prescribed by our FMR.

Fig. 12 shows the results obtained for variation P, with $\sigma_Z = 0.15$. This is the most pessimistic case considered in this work. Variation P features the lowest $Z_{max} = 1.5 \times 10^{-3}$, leading to an even more dramatic cut in the metallicity distribution, with respect to the previous case shown. As a consequence, the rate ends up being more than four orders of magnitude lower than in the previous case. Moreover, the rate peak shifts to a lower metallicity, just above 10^{-3}, reflecting the trend of the dN_{PISN}/dM_{SFR} over metallicity (variation P in Fig. 5). The mass distribution gets shifted towards lower values, favouring galaxies with $M_\star$ between 10^8 and 10^9 $M_\odot$. This is again due to the correlation between $M_\star$ and Z, given the lower Z_{max} cut. Since Z_{max} is far below the SFRD peak, a major contribution to the PISN rate is taken out of the game. This is the reason why in this variation the rate experiences such a dramatic decrease, as discussed in Sections 3.1 and 3.2.

Finally, in Fig. 13, we present the host galaxy properties obtained for variation O, combined with $\sigma_Z = 0.35$. As already discussed, here Z_{max} is greater than the SFRD peak, thus the rate is increased with respect to the fiducial case, by a factor less than one order of magnitude. Moreover, the peaks in both the Z and $M_\star$ distributions resemble the SFR ones since, differently from the previous cases shown, here the main contribution to the SFR is almost fully included in the PISN rate distribution. In particular, the peak lies at Z between 10^{-2} and $10^{-2.5}$, and $M_\star \lesssim 10^{10}$ $M_\odot$.

In all cases, prescribing a redshift dependence of α_{SMF} increases the rate at $M_\star \lesssim 10^{10}$ $M_\odot$, as can be seen by the grey band in the top panel. Indeed, the $\alpha_{SMF}(z)$ variation produces more galaxies with low mass with respect to the fixed α_{SMF} case (Fig. 1). Because of the correlation between $M_\star$ and Z, these galaxies will also be metal poor, explaining why the PISN rate slightly increases at metallicities below the SFRD peak (grey band in the lower right panel).

4 DISCUSSION

4.1 PISN rate and variations

Our results indicate that using different stellar evolution prescriptions, and varying the relevant parameters of the galactic model, hugely affects the PISN rate. Different stellar evolution codes, M_{CO} criteria and IMF upper limits produce a $\sim$ three orders of magnitude range from the most pessimistic to optimistic case (variations P and O in Fig. 6). These variations play a crucial role through the quantity Z_{max}, and secondly through the height of the dN_{PISN}/dM_{SFR} curve. As shown in Fig. 8, the interplay between Z_{max} and σ_Z

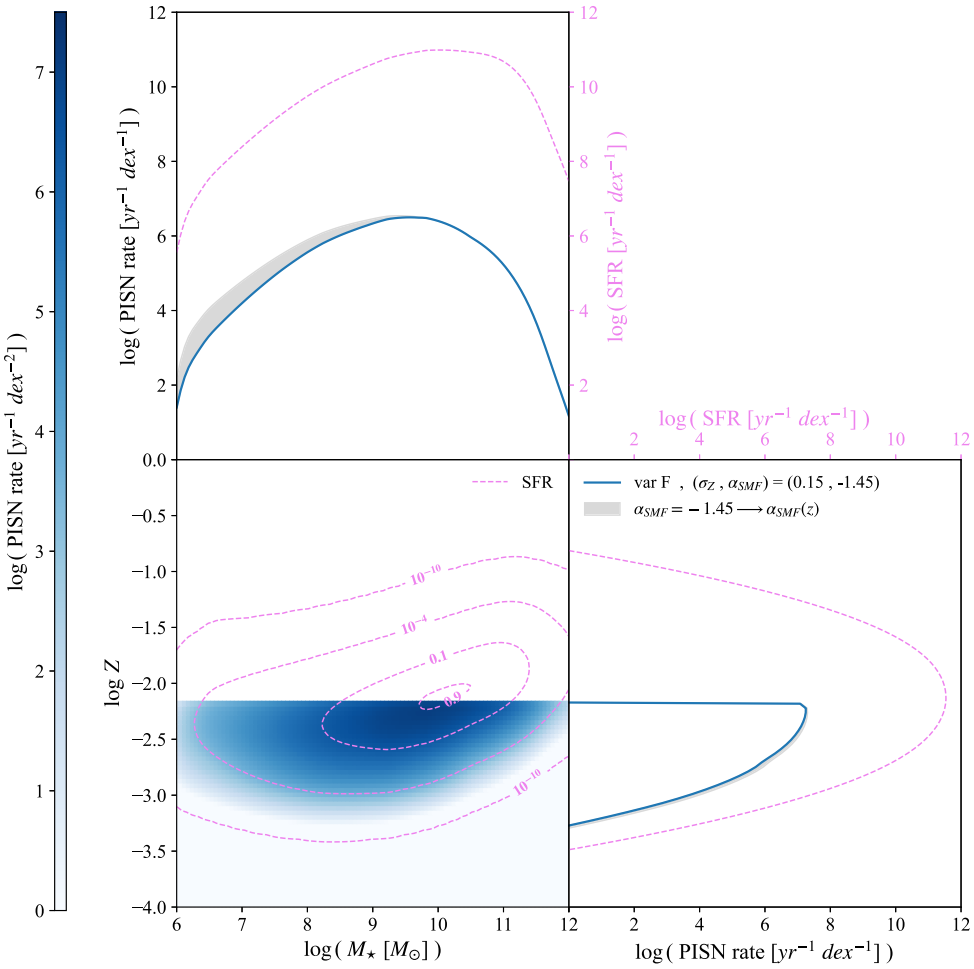

Figure 11. PISN rate as a function of $M_\star$, Z, and both, for our fiducial stellar variation (PARSEC-I, $M_{CO} \in [55 - 110]\,M_\odot$, $M_{IMF}^{up} = 300 M_\odot$), with $\sigma_Z = 0.15$ and $\alpha_{SMF} = -1.45$. Bands indicate the transition from the constant α_{SMF} to the $\alpha_{SMF}(z)$ case. For comparison, we also show the SFR contour levels as a function of $M_\star$ and Z for the corresponding variations, with fixed $\alpha_{SMF} = -1.45$, as well as the individual dependencies of the SFR on $M_\star$ and Z (dashed lines). In particular, we show the contours at 10^{-10}, 10^{-4}, 0.1, and 0.9 the SFR peak. As stressed in the text, these rates represent the contribution coming from all redshifts up to $z = 6$ (see equation 9).

broadens the PISN rate range to between $\sim$ five and seven orders of magnitude, throughout the whole redshift range considered. Indeed, Z_{max} completely cuts the SFRD distribution over metallicity, thus σ_Z strongly regulates the amount of SFRD which gets saved or lost (Fig. 7). This effect becomes huge for low Z_{max}. For example, in variation P, the peak of the PISN rate drops from $\sim 10^1$ to 10^{-1} Gpc^{-3}yr^{-1}, by decreasing σ_Z from 0.35 to 0.15. Moreover, the PISN rate peak is moved from $z \lesssim 2$ to $\gtrsim 3$, for the most pessimistic variation. Finally, varying α_{SMF} increases the PISN rate at $z > 3 - 4$ by a factor less than one order of magnitude, and shifts its peak to even higher redshifts than the constant-α_{SMF} case, up to $z \sim 4 - 5$ (Fig. 9).

These results show how the existing uncertainties in stellar and galaxy evolution hamper the determination of the cosmic PISN rate, with uncertainties dominated by the interplay between Z_{max} and σ_Z. On the other hand, this offers the opportunity to constrain stellar and galactic models, thanks to possible PISN observations in the future. Also in the eventuality that PISNe are never discovered, their lack of observations would help pose limits on the models' parameters.

According to our PISN rate distributions over galactic $M_\star$ and Z, the stellar mass of the favourable PISN host galaxies ranges from $10^8 - 10^9$ M$_\odot$, to around 10^{10} M$_\odot$, going from pessimistic to optimistic variation. Favoured galaxy metallicities range from $\sim 10^{-3}$ to just below 10^{-2}, following Z_{max}. These results tell us about the galactic environments which are most favourable to host PISNe, and can be taken as indication for current and future surveys aimed at observing these transients.

4.2 Comparison with previous works

It is useful to compare our results with previous works that, similarly to us, compute the PISN rate by combining a stellar evolution code with a cosmic star formation history and Z-evolution recipe (Stevenson et al. 2019; Buisson et al. 2020; Briel et al. 2022; Hendriks et al. 2023; Tanikawa et al. 2023; Tanikawa 2024). We note that, in all these comparisons, stellar and galactic prescriptions were selected in order to be as compatible as possible. Moreover, these works also consider PISNe arising from binary stars, while we only consider single stars. As we will discuss in the next section, we do not expect taking binaries into account to influence the PISN rate significantly. The Z-dependent SFRDs adopted in the following works exhibit σ_Z equal, or roughly compatible, to our $\sigma_Z = 0.35$ choice. Therefore, we compare with the results shown

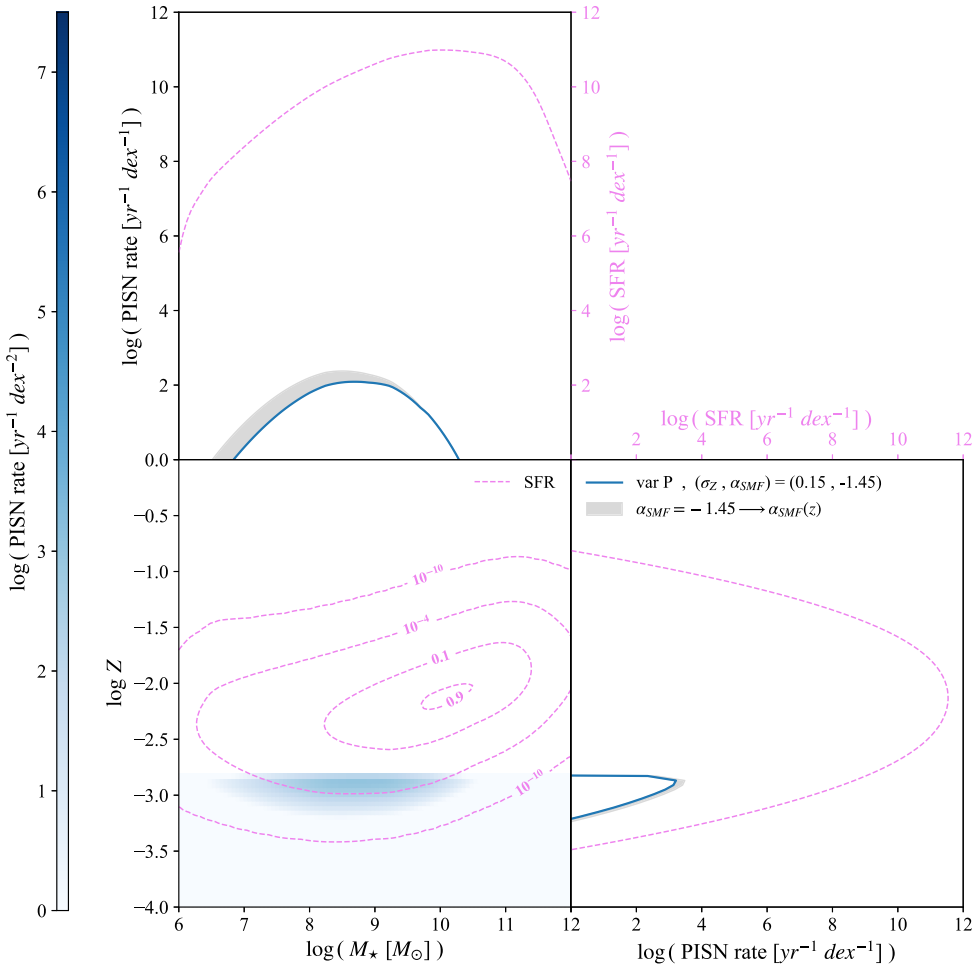

Figure 12. As in Fig. 11, for our pessimistic variation (FRANEC, $M_{CO} \in [60 - 105]\,M_\odot$, $M_{IMF}^{up} = 150 M_\odot$), with $\sigma_Z = 0.15$. Notice the different axis ranges for the PISN rate, due to the low values.

in Fig. 6, where we apply stellar variations keeping $\sigma_Z = 0.35$ fixed.

Overall, these previous determinations tend to fall in the lower end of our Fig. 6 range. This is partially due to the employed stellar evolution codes, producing different $dN_{PISN}/dM_{SFR}(Z)$ with respect to our work. Moreover, the interplay between $dN_{PISN}/dM_{SFR}(Z)$ and the adopted Z-evolution prescription can greatly enhance the differences with our results. Remarkably, the PISN rate obtained by Stevenson et al. (2019) extends up to three orders of magnitude downwards our pessimistic case (variation P in Fig. 6). Indeed, on one hand their $dN_{PISN}/dM_{SFR}(Z)$ is between one and two orders of magnitude lower than in our variation P, at metallicities crucial for the PISN rate, close to $Z_{max} \sim 2 \times 10^{-3}$ (compare our Fig. 5 with their fig. 2). This is also due to the fact that they consider an IMF upper limit of 150 $M_\odot$. Secondly, their galaxy metallicity distribution declines much more steeply in redshift with respect to ours. As explained in Sections 3.1 and 3.2 for our results, this can dramatically lower the PISN rate, besides favouring the contribution from higher redshifts. Interestingly, this is the same reason why, for example, in Tanikawa et al. (2023),the PISN rate turns out to peak at much higher redshifts than ours, around $z \sim 6 - 7$. As already discussed, we obtain the same effect, albeit of smaller entity, by adopting a GSMF low-mass end slope varying with redshift, $\alpha_{SMF} = \alpha_{SMF}(z)$, producing a steeper decrease of the galaxy metallicity with redshift, and causing the PISN rate to peak up to $z \sim 4 - 5$ (see Section 3.2). If we change the Curti et al. (2020) FMR prescription adopted here to that of Mannucci et al. (2010),we are even able to move the peak to $z > 6$, as discussed below (Section 4.5). Therefore, a redshift dependence of α_{SMF} might motivate the employment of steeper Z-evolution prescriptions.

Noticeably, while like us most of previous works focus on $Z \geq 10^{-5} - 10^{-4}$, Tanikawa et al. (2023) and Tanikawa (2024) also consider very low metallicity, Pop III stars. As a result, for example, in Tanikawa (2024) the PISN rate features two distinct peaks, one around $z = 2 - 3$ due to Pop II/I stars, and the other at $z \gtrsim 12$ due to Pop III. Depending on the considered variations, including different IMF upper limits, Tanikawa et al. (2023) and Tanikawa (2024) find these two peak contributions to be roughly compatible, or the Pop III one to be dominant. We further discuss the contribution to the PISN rate from Pop III stars below.

4.3 PI/CC ratio

In Section 3.3, we computed the ratio between PISN and CCSN rate, for our $Z_{max} - \sigma_Z$ combinations (see Table 3). Our range of results exhibits an upper limit $\gtrsim 10^{-2}$, which is close to the value typically considered in the literature, coming from the simple integration of the IMF over the expected PISN and CCSN progenitor mass ranges.

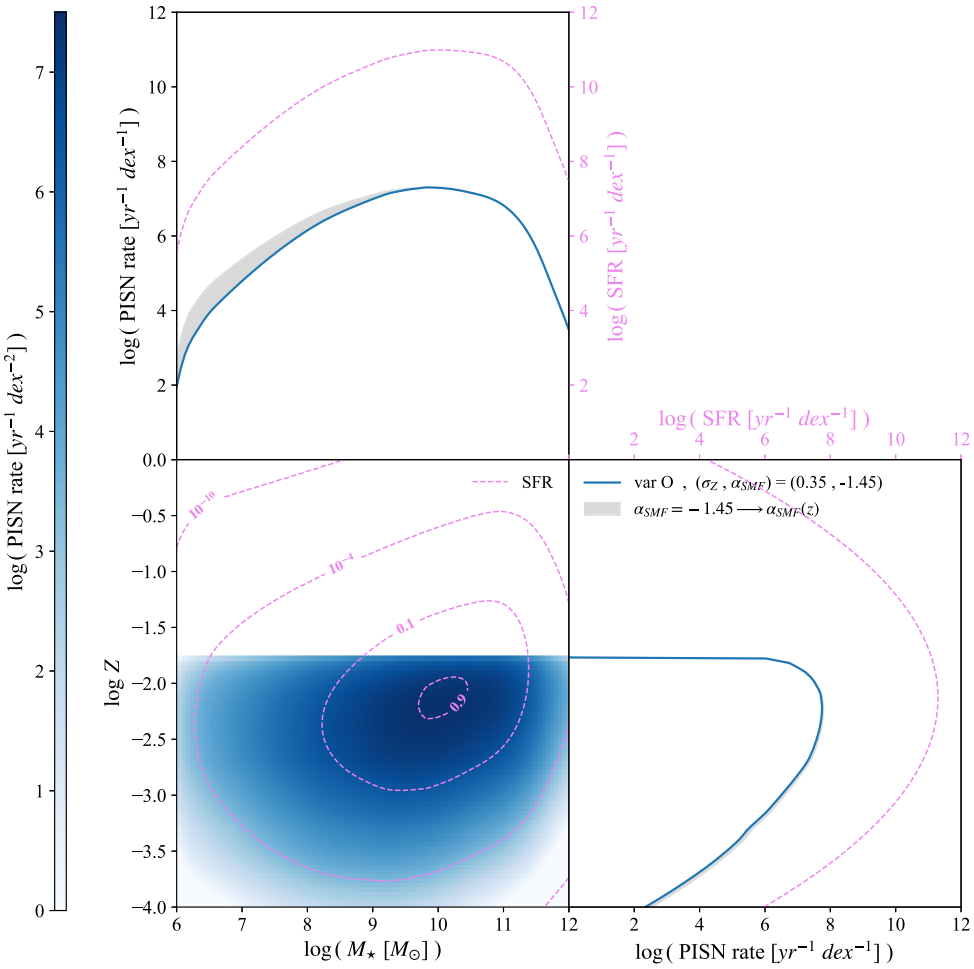

Figure 13. As in Fig. 11, for our optimistic variation (PARSEC-II, $M_{CO} \in [45 - 120]$ $M_\odot$, $M^{up}_{IMF} = 300 M_\odot$), with $\sigma_Z = 0.35$.

Adopting our Kroupa IMF, and integrating over the typical $[140 - 260]$ $M_\odot$ range for PISN, and $[8 - 50]$ $M_\odot$ for CCSN, gives a value of $\sim 1.5 \times 10^{-2}$ for the PI/CC ratio. Considering the hundreds of observed CCSNe, and neglecting the different observational biases linked to these transients for the sake of simplicity, this would lead to expect at least 1 PISN detection so far, which is not the case. On the other hand, the lowest part of our range would tell us that PISNe are simply too rare with respect to CCSNe, making it trivial to understand why we never observed one. We stress that the differences in PISN and CCSN observation can be crucial and must be taken into account in order to make more robust statements.

Using the missed PISN observation as a constraint, it is possible to infer an upper limit on the PI/CC ratio, as done in Nicholl et al. (2013). They obtain a PI/CC ratio $< 6 \times 10^{-6}$ within $z < 0.6$ (at 3σ), which is compatible with the lowest part of our range. Studies of this kind can be extremely valuable in constraining the parameters of stellar and galaxy evolution models, by excluding all parameter values that produce too high PI/CC ratios. However, these studies would inevitably suffer from important degeneracies. We leave a more accurate assessment regarding these matters to the follow-up work.

4.4 PISNe in binaries

As already outlined, so far we only considered PISNe arising from single stars, under the assumption that interactions in binaries (e.g. mass transfer) do not affect significantly the rate of PISN occurrence. In order to test this assumption, we run the most recent version of the SEVN code (Iorio et al. 2022) to generate a synthetic population of binary stars. We then generate a population of single stars, and compute the dN_{PISN}/dM_{SFR} for both populations. By assuming that a fraction $f_{bin} = 0.5$ of stars lie in binaries, we are able to compute the fraction of PISNe arising in binaries with respect to single stars, f^{PISN}_{bin}.

We get $f^{PISN}_{bin} = 0.56$, meaning that PISN events are distributed roughly equally among single stars and binaries. Indeed, we find that stellar mergers are the dominant process varying the masses of stars, while other processes such as common envelope and Roche lobe overflow only play a secondary role. The number of stars entering and exiting the PISN mass range, by merging with another star, roughly balance each other. f_{bin} is slightly in favour of binaries due to our bottom-heavy IMF, making it so that stars with lower mass which merge into the PISN range are more abundant than higher mass stars merging out of that range.

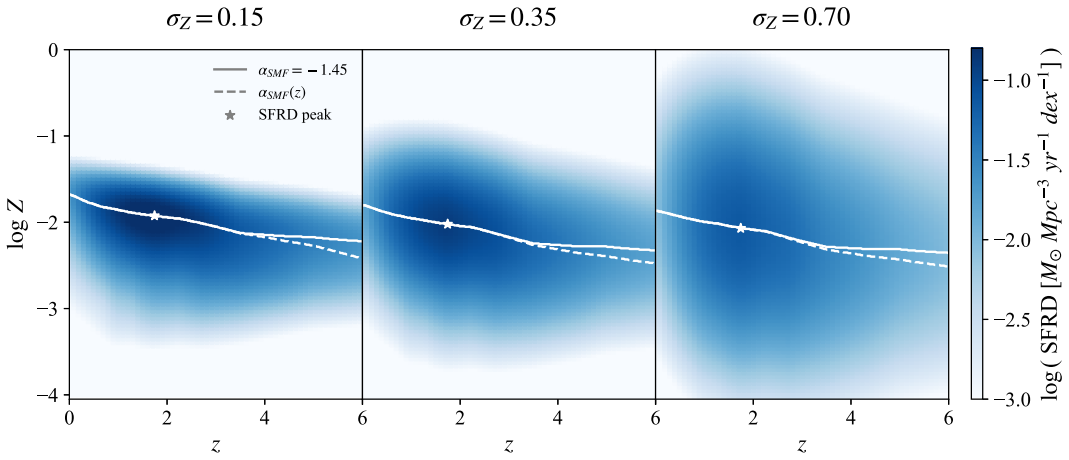

Figure 14. As Fig. 3, for the Mannucci et al. (2010) FMR.

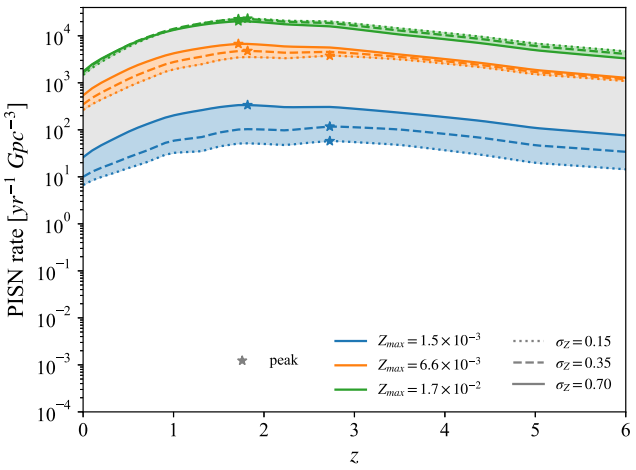

Figure 15. As Fig. 8, for the Mannucci et al. (2010) FMR.

We stress that this computation requires an assumption on $f_{\rm bin}$, which is still quite uncertain (e.g. Sana et al. 2012). None the less, we regard $f_{\rm bin} = 0.5$ as a fiducial value, based on what established so far in the literature.

4.5 FMR variation

In this work, we adopted the FMR from Curti et al. (2020), one of the most recent determinations (see Section 2.1). As we saw, this prescription leads to a drop in the Z-dependent SFRD at $z \lesssim 1$, at metallicities crucial for PISN production (Fig. 3), causing the PISN rate to drop at $z \lesssim 1$ (e.g. Fig. 8). It is useful to consider an alternative FMR, in order to see how dependent our results are on this relation. We choose to follow Mannucci et al. (2010), who present the following fit:

$$12 + \log(O/H) = 8.90 + 0.37m - 0.14s - 0.19m^2 + 0.12ms - 0.054s^2, \quad (10)$$

where $m = \log(M_\star) - 10$ and $s = \log(SFR)$. Here, $\log Z = 12 + \log(O/H) - 10.58$, as in Boco et al. (2021). In the following, we will address Curti et al. (2020) as C20, and Mannucci et al. (2010) as M10.

Fig. 14 shows the Z-dependent SFRD obtained by adopting the M10 FMR, for $\sigma_{\rm Z} = [0.15, 0.35, 0.70]$ and $\alpha_{\rm SMF} = -1.45$, to be compared with Fig. 3 for the C20 one. We show in Fig. 15, the PISN rate we obtain for the same $Z_{\rm max} - \sigma_{\rm Z}$ combinations as Fig. 8. One can clearly see how this new FMR strongly reduces our range of results, which now sums up to just two/three orders of magnitude, as opposed to the five/seven orders of magnitude of Fig. 8. This is due to the fact that, for $\sigma_{\rm Z} = 0.15$ and 0.35, the SFRD computed with the M10 FMR extends to lower metallicities, past $Z = 10^{-3}$, with respect to the one computed with the C20 FMR. This is due to the steeper dependence of galaxy metallicity with stellar mass found in M10 (see also fig. 3 in C20). As a consequence, the PISN rate contribution coming from those metallicities is enhanced, as can be seen in Fig. 16. Since this is where $Z_{\rm max}$ lies for our most pessimistic variations (Fig. 5), the corresponding PISN rate is especially enhanced. Remarkably, in the case with $Z_{\rm max} = 1.5 \times 10^{-3}$ and $\sigma_{\rm Z} = 0.15$ (lowest curve in Figs 8 and 15), the difference in rate due to the FMR variation amounts to two/three orders of magnitude, reaching more than four orders of magnitude at $z = 0$. On the other hand, in the case with $\sigma_{\rm Z} = 0.70$ the PISN rate does not vary significantly since, as can be seen in the right panels of Figs 3 and 14, the SFRD distribution is quite similar in the two FMR variations. Moreover, the $\alpha_{\rm SMF} = \alpha_{\rm SMF}(z)$ variation produces an even steeper decrease of galaxy metallicity with redshift, with respect to the Curti et al. (2020) FMR case. As a consequence, the PISN rate peak is brought to even higher redshifts, past $z = 6$, as shown in Fig. 17.

This warns us about how dependent the PISN rate can be on the adopted FMR. Our results must thus be taken with caution. We stress how it is the lowest end of this range to be affected, while its upper end appears to be immune. It again becomes clear how crucial the interplay between $Z_{\rm max}$ and $\sigma_{\rm Z}$ is in determining the PISN rate, it being the cause of these delicate dependencies.

4.6 PISNe from Pop III stars

It is traditionally believed that only low-Z stars explode as PISNe. For this reason, due to their extremely low metallicities $Z \lesssim 10^{-10}$ (e.g. Cassisi & Castellani 1993), very massive Population III stars are usually considered as main PISN progenitors (e.g. El Eid et al. 1983; Ober et al. 1983; Baraffe et al. 2001; Fryer, Woosley & Heger 2001; Umeda & Nomoto 2001; Heger & Woosley 2002; Scannapieco et al. 2005; Wise & Abel 2005; Langer et al. 2007; Kasen et al. 2011; Dessart et al. 2012; Pan et al. 2012; Yoon et al. 2012; Whalen

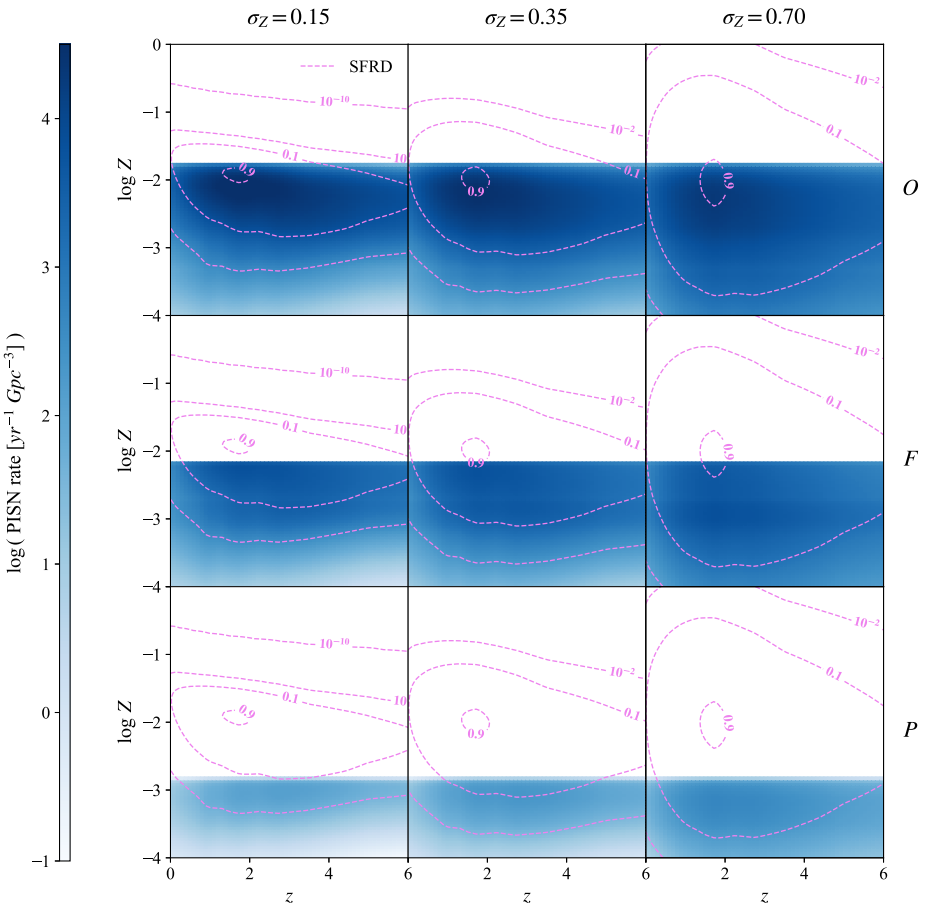

Figure 16. As Fig. 7, for the Mannucci et al. (2010) FMR.

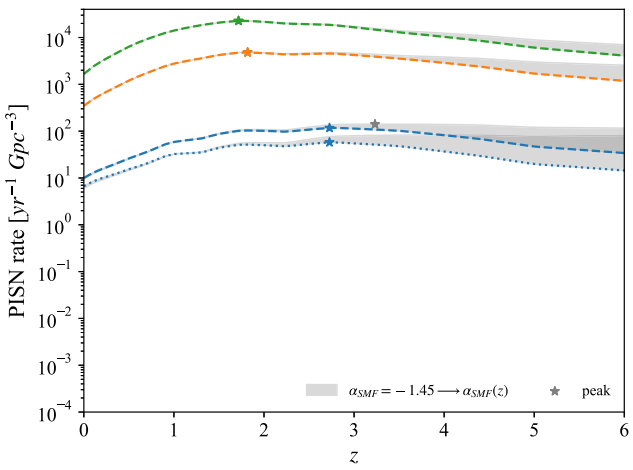

Figure 17. As in Fig. 9, for the Mannucci et al. (2010) FMR.

et al. 2013; de Souza et al. 2013; Souza et al. 2014; Whalen et al. 2014; Smidt et al. 2015; Magg et al. 2016; Venditti et al. 2024; Bovill et al. 2024; Wiggins et al. 2024). On the other hand, our stellar evolution tracks and $M_{\rm CO}$ variations allow for PISNe up to $\sim$ solar metallicity, $\sim 1.7 \times 10^{-2}$ for variation O. Combining with the SFRD, we find that the main PISN rate contribution comes from $Z \sim 10^{-3} - 10^{-2}$, typical of Pop II/I stars. This result identifies Pop II/I stars as prominent PISN candidates. However, we stress that in this work we only consider $Z \geq 1 \times 10^{-4}$ and $z \leq 6$. In order to study the contribution to the PISN rate coming from Pop III stars, and make a comparison with that from Pop II/I, one would need to extend the treatment to lower metallicities and higher redshifts. This task is hindered by the uncertainties surrounding relevant quantities like the Pop III SFRD and IMF, due to the lack of Pop III observations and the overall challenges of searching those very high redshifts. None the less, we attempt at estimating the PISN rate contribution from Pop III stars, and compare it with our results for Pop II/I.

We compute the Pop III PISN rate analogously as in equation (1). In particular, we consider the $Z = 10^{-11}$PARSEC stellar evolution tracks, introduced in Costa et al. (2023) inside the framework of SEVN. For the Pop III SFRD, we consider the determination by Hartwig et al. (2022, see also Santoliquido et al. 2023), obtained with the semi-analitical model A-SLOTH (Ancient Stars and Local Observables by Tracing Halos). Pop III stars are believed to follow a more top-heavy IMF with respect to Pop II/I, that might extend up to 1000 $M_\odot$ (e.g. Hirano et al. 2015). This motivates us to adopt a Larson IMF (Larson 1998) of the form $\propto M^{\xi}\, e^{-M_c/M}$ (where $M \equiv M_{\rm ZAMS}$), defined up to 1000 $M_\odot$, with Kroupa-like slope $\xi = -2.3$, and characteristic mass $M_c = 30\,M_\odot$. We note that varying the upper mass limit from 1000 to 300 $M_\odot$ does not affect the results, since the $Z = 10^{-11}$ tracks we use predict a PISN progenitor mass range of $\sim [107 - 223]\,M_\odot$. Finally, we vary $M_{\rm CO}$ criterion for PISN as done in the rest of the work.

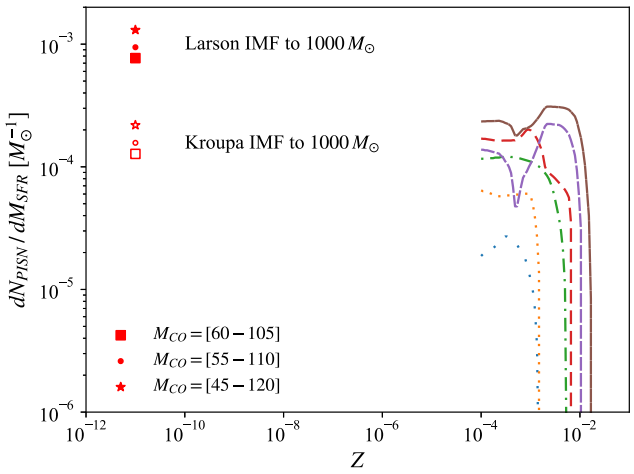

Figure 18. Number of PISNe per unit star-forming mass produced by Pop III stars with $Z = 10^{-11}$, adopting a Larson IMF up to 1000 $M_\odot$ (filled markers). We also show the case of a Kroupa IMF defined up to 1000 $M_\odot$ (empty markers). We indicate the M_{CO} variations with different shapes. For comparison, on the right is shown the same plot as in Fig. 5.

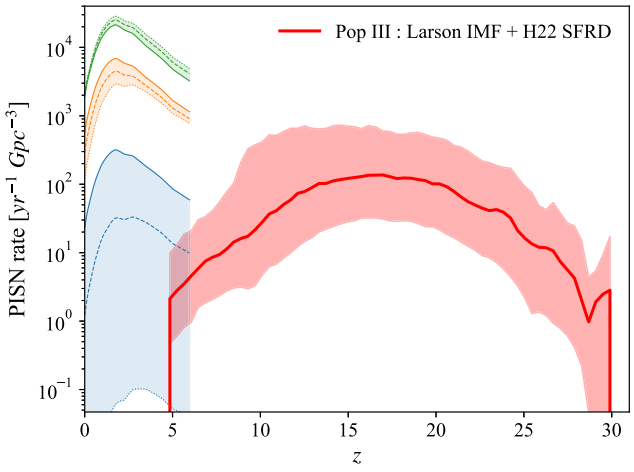

Figure 19. PISN rate from Pop III stars as a function of redshift, computed by adopting a Larson IMF and the Pop III SFRD determination by Hartwig et al. (2022). The band indicates the uncertainty coming from the 95 per cent credible interval of the Hartwig et al. (2022) SFRD, as computed in Santoliquido et al. (2023). For clarity, we fix the fiducial, $M_{CO} = [55 - 110]$ $M_\odot$ variation. On the left we report the results obtained for Pop II/I stars, as in Fig. 8, for comparison.

In Fig. 18, we show the dN_{PISN}/dM_{SFR} obtained with our Larson IMF, compared to the case of a Kroupa IMF defined up to 1000 $M_\odot$. As one can see, the Kroupa IMF produces a Pop III dN_{PISN}/dM_{SFR} comparable to the Pop II/I one for the most optimistic stellar variations. On the contrary, the more top-heavy, Larson IMF elevates this quantity by almost an order of magnitude. Indeed, the Larson IMF increases the relative abundance of stars with masses in the PISN range, compared to the Kroupa IMF. Since this result depends only slightly on the chosen M_{CO} criterion, we fix it to the fiducial case in computing the PISN rate, that we show in Fig. 19 for the Larson IMF. As one can see, the Pop III PISN rate lies around the same values of the most pessimistic results obtained for Pop II/I. Indeed, even though the Hartwig et al. (2022) Pop III SFRD is orders of magnitude lower than the one employed in this work for Pop II/I stars, the Larson IMF produces more PISNe per unit mass compared to the Kroupa IMF (Fig. 18). Moreover, the inclusion of the whole SFRD contribution in $Z = 10^{-11}$, allows to avoid the metallicity cut due to Z_{max} which, as discussed in depth in the paper, can lower significantly the PISN rate, especially in the lowest σ_Z cases.

Previous Pop III PISN rate determinations in the literature tend to distribute in the middle/upper range of our results for Pop II/I stars (Fig. 8), with some even reaching our most optimistic results (Scannapieco et al. 2005; Wise & Abel 2005; Pan et al. 2012; de Souza et al. 2013; Souza et al. 2014; Magg et al. 2016; Regős et al. 2020; Tanikawa et al. 2023; Venditti et al. 2024; Tanikawa 2024; Wiggins et al. 2024). All in all, despite the uncertainties on the Pop III SFRD and IMF, these considerations suggest that Pop III could somewhat contribute to the PISN rate at $z \gtrsim 6$.

5 CONCLUSIONS

In this work, we compute the PISN rate as a function of redshift up to $z = 6$, by combining stellar evolution tracks with a semi-empirical determination of the metallicity-dependent cosmic star formation history. The aim is to study how the uncertainties in both stellar and galaxy evolution theory affect our knowledge about the rate of PISN occurrence throughout cosmic history. We vary stellar evolution code, M_{CO} criterion to have PISN, and IMF upper limit, as well as the dispersion of the galaxy metallicity distribution and the low-mass end slope of the GSMFs. We find these variations to have a huge effect on our results. The PISN rate spans roughly three orders of magnitude under stellar variations. Their effect can be boiled down to the dependence on the maximum metallicity to have PISN, Z_{max}, and the height of the dN_{PISN}/dM_{SFR} curve. Remarkably, the interplay between Z_{max} and σ_Z can extend the PISN rate range up to $\sim$ seven orders of magnitude, depending on redshift. The local, $z = 0$ rate ranges from 4×10^{-4} to 2×10^3 yr^{-1} Gpc^{-3}, while the values at peak range from $\sim 10^{-1}$ to 3×10^4 yr^{-1} Gpc^{-3}. Moreover, prescribing a redshift dependence of α_{SMF} increases the PISN rate at $z > 3 - 4$. Also the position of the peak gets affected, shifting from $z \lesssim 2$ up to $z \sim 4 - 5$ throughout all variations. This warns us about the delicate link between these two metallicity parameters, in choosing stellar evolution prescriptions and IMF leading to a certain Z_{max}, and in adopting recipes for the cosmic metallicity distribution of galaxies.

All in all, our limited knowledge makes the PISN rate very uncertain. On the other hand, the strong dependencies we find offer the chance to constrain these parameters based on possible PISN observations in the future, or the lack of PISN observations in the eventuality that these transients are never discovered. Even accounting for the significant degeneracies, this would help dispel the uncertainties around massive star evolution, such as the criterion for a star to undergo pair instability and the maximum stellar mass, and the evolution of star formation and galaxy metallicity throughout cosmic history. We will delve into these aspects in a follow-up work, dedicated to studying PISN detection with telescopes such as *JWST*, in which we will attempt at answering the question why PISN explosions have never been observed.

Our fiducial model indicates galaxies with stellar masses between $\sim 10^9$ and $10^{10} M_\odot$, and metallicities $\lesssim 10^{-2}$, to be the favourable PISN hosts, providing the main contribution to the PISN rate. These values shift to $M_\star \sim 10^8 - 10^9$ $M_\odot$ and $Z \gtrsim 10^{-3}$ in our most pessimistic variation, and to $M_\star \sim 10^{10}$ $M_\odot$ and $Z \sim 10^{-2}$ in our most

optimistic one. This can represent useful information for the design of current and future campaigns aimed at observing these elusive transients, with facilities such as *JWST*, the *Vera Rubin Observatory*, *Euclid*, the *Nancy Grace Roman Space Telescope*, the *Zwicky Transient Facility*, and *ULTIMATE-Subaru* (e.g. Weinmann & Lilly 2005; Whalen et al. 2012; Kozyreva et al. 2014a; Smidt et al. 2015; Hartwig et al. 2018; Moriya et al. 2019, 2022a; Regős et al. 2020; Moriya, Quimby & Robertson 2022b; Tanikawa et al. 2023; Tanikawa 2024).

Finally, our stellar evolution tracks and M_{CO} variations allow stars to explode as PISNe up to $\sim$ solar metallicity. As a consequence, we find peak metallicities for the PISN rate that suggest Pop II/I stars to be prominent PISN progenitors. This goes against the traditional expectation that PISNe come exclusively or preferentially from very low metallicity, Pop III stars, a point which is worth exploring in the future.

ACKNOWLEDGEMENTS

The authors thank the anonymous referee for constructive comments, and Max Briel and David Hendriks for helpful discussions. This work was partially funded from the projects: 'Data Science methods for MultiMessenger Astrophysics and Multi-Survey Cosmology' funded by the Italian Ministry of University and Research, Programmazione triennale 2021/2023 (DM n.2503 dd. 9 December 2019), Programma Congiunto Scuole; EU H2020-MSCA-ITN-2019 n. 860744 *BiD4BESt: Big Data applications for black hole Evolution STudies*; Italian Research Center on High Performance Computing Big Data and Quantum Computing (ICSC), project funded by European Union – NextGenerationEU – and National Recovery and Resilience Plan (NRRP) – Mission 4 Component 2 within the activities of Spoke 3 (Astrophysics and Cosmos Observations); European Union – NextGenerationEU under the PRIN MUR 2022 project no. 20224JR28W 'Charting unexplored avenues in Dark Matter'; INAF Large 'grant 2022 funding scheme with the project 'MeerKAT and LOFAR Team up: a Unique Radio Window on Galaxy/AGN co-Evolution; INAF GO-GTO Normal 2023 funding scheme with the project 'Serendipitous H-ATLAS-fields Observations of Radio Extragalactic Sources (SHORES)'. The authors declare no conflict of interest.

DATA AVAILABILITY

The data used in this work can be made available upon request.

REFERENCES

Abbot B. P., et al., 2016, Phys. Rev. Lett., 116, 061102
Abbot R., et al., 2020, Phys. Rev. Lett., 125, 101102
Aguado D. S. et al., 2023, MNRAS, 520, 866
Aoki W., Tominaga N., Beers T. C., Honda S., Lee Y. S., 2014, Science, 345, 912
Artale M. C., Mapelli M., Giacobbo N., Sabha N. B., Spera M., Santoliquido F., Bressan A., 2019, MNRAS, 487, 1675
Asplund M., Grevesse N., Sauval A. J., Scott P., 2009, ARA&A, 47, 481
Ballero S. K., Matteucci F., Chiappini C., 2006, New Astron., 11, 306
Baraffe I., Heger A., Woosley S. E., 2001, ApJ, 550, 890
Barkat Z., Rakavy G., Sack N., 1967, Phys. Rev. Lett., 18, 379
Belczynski K., 2020, ApJ, 905, L15
Belczynski K., Holz D. E., Bulik T., O'Shaughnessy R., 2016a, Nature, 534, 512
Belczynski K. et al., 2016b, A&A, 594, A97
Bestenlehner J. M. et al., 2020, MNRAS, 499, 1918
Bisnovatyi-Kogan G. S., Kazhdan Y. M., 1967, Sov. Astron., 10, 604
Boco L., Lapi A., Goswami S., Perrotta F., Baccigalupi C., Danese L., 2019, ApJ, 881, 157
Boco L., Lapi A., Chruslinska M., Donevski D., Sicilia A., Danese L., 2021, ApJ, 907, 110
Botticella M. T. et al., 2007, A&A, 479, 49
Botticella M. T., Smartt S. J., Kennicutt R. C., Cappellaro E., Sereno M., Lee J. C., 2012, A&A, 537, A132
Bouwens R. J. et al., 2021, AJ, 162, 47
Bovill M. S., Stiavelli M., Wiggins A. I., Ricotti M., Trenti M., 2024, ApJ, 962, 49
Brands S. A. et al., 2022, A&A, 663, A36
Bressan A., Marigo P., Girardi L., Salasnich B., Cero C. D., Rubele S., Nanni A., 2012, MNRAS, 427, 127
Briel M. M., Eldridge J. J., Stanway E. R., Stevance H. F., Chrimes A. A., 2022, MNRAS, 514, 1315
Briel M. M., Stevance H. F., Eldridge J. J., 2023, MNRAS, 520, 5724
du Buisson L. et al., 2020, MNRAS, 499, 5941
Caffau E., Ludwig H.-G., Steffen M., Freytag B., Bonifacio P., 2010, Sol. Phys., 268, 255
Caffau E. et al., 2022, MNRAS, 518, 3796
Cao L., Lu Y., Zhao Y., 2017, MNRAS, 474, 4997
Cappellaro E. et al., 2005, A&A, 430, 83
Casey C. M. et al., 2018, ApJ, 862, 77
Cassisi S., Castellani V., 1993, ApJS, 88, 509
Chatzopoulos E., Wheeler J. C., 2012, ApJ, 748, 42
Chatzopoulos E., Gilmer M. S., Wollaeger R. T., Fröhlich C., Even W. P., 2019, ApJ, 875, 140
Chen Y., Girardi L., Bressan A., Marigo P., Barbieri M., Kong X., 2014, MNRAS, 444, 2525
Chen Y., Bressan A., Girardi L., Marigo P., Kong X., Lanza A., 2015, MNRAS, 452, 1068
Cherchneff I., Dwek E., 2009, ApJ, 703, 642
Cherchneff I., Dwek E., 2010, ApJ, 713, 1
Chieffi A., Limongi M., 2013, ApJ, 764, 21
Chruslinska M., Nelemans G., 2019, MNRAS, 488, 5300
Chruślińska M., Nelemans G., Boco L., Lapi A., 2021, MNRAS, 508, 4994
Cooke J. et al., 2012, Nature, 491, 228
Costa G., Girardi L., Bressan A., Marigo P., Rodrigues T. S., Chen Y., Lanza A., Goudfrooij P., 2019, MNRAS, 485, 4641
Costa G., Bressan A., Mapelli M., Marigo P., Iorio G., Spera M., 2021, MNRAS, 501, 4514
Costa G., Mapelli M., Iorio G., Santoliquido F., Escobar G. J., Klessen R. S., Bressan A., 2023, MNRAS, 525, 2891
Crowther P. A., 2019, Galaxies, 7, 88
Crowther P. A., Schnurr O., Hirschi R., Yusof N., Parker R. J., Goodwin S. P., Kassim H. A., 2010, MNRAS, 408, 731
Crowther P. A. et al., 2016, MNRAS, 458, 624
Curti M., Mannucci F., Cresci G., Maiolino R., 2020, MNRAS, 491, 944
Dahlen T. et al., 2004, ApJ, 613, 189
Dahlen T., Strolger L.-G., Riess A. G., Mattila S., Kankare E., Mobasher B., 2012, ApJ, 757, 70
Dessart L., Waldman R., Livne E., Hillier D. J., Blondin S., 2012, MNRAS, 428, 3227
Dunlop J. S. et al., 2016, MNRAS, 466, 861
El Eid M., Fricke K., Ober W., 1983, A&A, 119, 54
Elbert O. D., Bullock J. S., Kaplinghat M., 2017, MNRAS, 473, 1186
Eldridge J. J., Stanway E. R., Tang P. N., 2018, MNRAS, 482, 870
Evans C. J. et al., 2010, ApJ, 715, L74
Farmer R., Renzo M., de Mink S. E., Marchant P., Justham S., 2019, ApJ, 887, 53
Fowler W. A., Hoyle F., 1964, ApJ, 9, 201
Fraley S., 1968, Ap&SS, 2, 96
Fryer C. L., Woosley S. E., Heger A., 2001, ApJ, 550, 372
Gal-Yam A., 2012, Science, 337, 927
Gal-Yam A. et al., 2009, Nature, 462, 624
Gal-Yam A., Mazzali P. A., Manulis I., Bishop D., 2013, PASP, 125, 749

Gilmer M. S., Kozyreva A., Hirschi R., Fröhlich C., Yusof N., 2017, ApJ, 846, 100
Gomez S. et al., 2019, ApJ, 881, 87
Goswami S. et al., 2021, A&A, 650, A203
Goswami S. et al., 2022, A&A, 663, A1
Grafener G., Hamann W. R., 2008, A&A, 482, 945
Gruppioni C. et al., 2013, MNRAS, 432, 23
Gruppioni C. et al., 2020, A&A, 643, A8
Guillochon J., Parrent J., Kelley L. Z., Margutti R., 2017, ApJ, 835, 64
Hartwig T., Bromm V., Loeb A., 2018, MNRAS, 479, 2202
Hartwig T. et al., 2022, ApJ, 936, 45
Heger A., Woosley S. E., 2002, ApJ, 567, 532
Heger A., Fryer C. L., Woosley S. E., Langer N., Hartmann D. H., 2003, ApJ, 591, 288
Hendriks D. D., van Son L. A. C., Renzo M., Izzard R. G., Farmer R., 2023, MNRAS, 526, 4130
Higgins E. R., Sander A. A. C., Vink J. S., Hirschi R., 2021, MNRAS, 505, 4874
Hirano S., Hosokawa T., Yoshida N., Omukai K., Yorke H. W., 2015, MNRAS, 448, 568
Iorio G. et al., 2022, MNRAS, 524, 426
Jerkstrand A., Smartt S. J., Heger A., 2015, MNRAS, 455, 3207
Kalari V. M., Horch E. P., Salinas R., Vink J. S., Andersen M., Bestenlehner J. M., Rubio M., 2022, ApJ, 935, 162
Kasen D., Woosley S. E., Heger A., 2011, ApJ, 734, 102
Kinugawa T., Nakamura T., Nakano H., 2020, MNRAS, 501, L49
Kistler M. D., Yüksel H., Beacom J. F., Hopkins A. M., Wyithe J. S. B., 2009, ApJ, 705, L104
Kistler M. D., Yuksel H., Hopkins A. M., 2013, The Cosmic Star Formation Rate from the Faintest Galaxies in the Unobservable Universe, preprint (arXiv:1305.1630)
Kojima T. et al., 2021, ApJ, 913, 22
Koutsouridou I., Salvadori S., Skúladóttir Á., 2023, ApJL, 962, L26
Kozyreva A., Blinnikov S., 2015, MNRAS, 454, 4357
Kozyreva A., Blinnikov S., Langer N., Yoon S.-C., 2014a, A&A, 565, A70
Kozyreva A., Yoon S.-C., Langer N., 2014b, A&A, 566, A146
Kozyreva A. et al., 2016, MNRAS, 464, 2854
Kozyreva A., Kromer M., Noebauer U. M., Hirschi R., 2018, MNRAS, 479, 3106
Kroupa P., 2001, MNRAS, 322, 231
Lamberts A., Garrison-Kimmel S., Clausen D. R., Hopkins P. F., 2016, MNRAS, 463, L31
Lamberts A. et al., 2018, MNRAS, 480, 2704
Langer N., 2012, ARA&A, 50, 107
Langer N., Norman C. A., de Koter A., Vink J. S., Cantiello M., Yoon S.-C., 2007, A&A, 475, L19
Larson R. B., 1998, MNRAS, 301, 569
Li S.-S., Mao S., Zhao Y., Lu Y., 2018, MNRAS, 476, 2220
Limongi M., Chieffi A., 2018, ApJS, 237, 13
Liu D. et al., 2018, ApJ, 853, 172
Lunnan R. et al., 2016, ApJ, 831, 144
Madau P., Dickinson M., 2014, ARA&A, 52, 415
Magg M., Hartwig T., Glover S. C. O., Klessen R. S., Whalen D. J., 2016, MNRAS, 462, 3591
Mannucci F., Cresci G., Maiolino R., Marconi A., Gnerucci A., 2010, MNRAS, 408, 2115
Mapelli M., Giacobbo N., 2018, MNRAS, 479, 4391
Mapelli M., Giacobbo N., Ripamonti E., Spera M., 2017, MNRAS, 472, 2422
Marchant P., Moriya T. J., 2020, A&A, 640, L18
Marchant P., Renzo M., Farmer R., Pappas K. M. W., Taam R. E., de Mink S. E., Kalogera V., 2019, ApJ, 882, 36
Marigo P., Bressan A., Nanni A., Girardi L., Pumo M. L., 2013, MNRAS, 434, 488
Martinet S., Meynet G., Ekström S., Georgy C., Hirschi R., 2023, A&A, 679, A137
Matteucci F., Pipino A., 2005, MNRAS, 357, 489
Mattila S. et al., 2012, ApJ, 756, 111
Mazzali P. A., Moriya T. J., Tanaka M., Woosley S. E., 2019, MNRAS, 484, 3451
Melinder J. et al., 2012, A&A, 545, A96
Moriya T. J., Wong K. C., Koyama Y., Tanaka M., Oguri M., Hilbert S., Nomoto K., 2019, PASJ, 71, 59
Moriya T. J. et al., 2022a, A&A, 666, A157
Moriya T. J., Quimby R. M., Robertson B. E., 2022b, ApJ, 925, 211
Navarro-Carrera R., Rinaldi P., Caputi K. I., Iani E., Kokorev V., van Mierlo S. E., 2024, ApJ, 961, 207
Neijssel C. J. et al., 2019, MNRAS, 490, 3740
Nguyen C. T. et al., 2022, A&A, 665, A126
Nicholl M. et al., 2013, Nature, 502, 346
Nicholl M. et al., 2020, Nat. Astron., 4, 893
Novak M. et al., 2017, A&A, 602, A5
O'Shaughnessy R., Bellovary J. M., Brooks A., Shen S., Governato F., Christensen C. R., 2016, MNRAS, 464, 2831
Ober W., El Eid M., Fricke K., 1983, A&A, 119, 61
Olejak A., Fryer C. L., Belczynski K., Baibhav V., 2022, MNRAS, 516, 2252
Pan T., Kasen D., Loeb A., 2012, MNRAS, 422, 2701
Petrushevska T. et al., 2016, A&A, 594, A54
Planck Collaboration VI, 2020, A&A, 641, A6
Popesso P. et al., 2022, MNRAS, 519, 1526
Quimby R. M. et al., 2011, Nature, 474, 487
Rakavy G., Shaviv G., 1967, ApJ, 148 803
Regős E., Vinkó J., Ziegler B. L., 2020, ApJ, 894, 94
Ricotti M., Ostriker J. P., 2004, MNRAS, 350, 539
Rollinde E., Vangioni E., Maurin D., Olive K. A., Daigne F., Silk J., Vincent F. H., 2009, MNRAS, 398, 1782
Romano D., Matteucci F., Zhang Z.-Y., Papadopoulos P. P., Ivison R. J., 2017, MNRAS, 470, 401
Romano D., Matteucci F., Zhang Z.-Y., Papadopoulos P. P., Ivison R. J., 2020a, MNRAS, 499, 523
Romano D., Franchini M., Grisoni V., Spitoni E., Matteucci F., Morossi C., 2020b, A&A, 639, A37
Rowan-Robinson M. et al., 2016, MNRAS, 461, 1100
Sabhahit G. N., Vink J. S., Sander A. A. C., Higgins E. R., 2023, MNRAS, 524, 1529
Salvadori S., Bonifacio P., Caffau E., Korotin S., Andreevsky S., Spite M., Skuladottir A., 2019, MNRAS, 487, 4261
Sana H. et al., 2012, Science, 337, 444
Sander A. A. C., Hamann W. R., Todt H., Hainich R., Shenar T., Ramachandran V., Oskinova L. M., 2019, A&A, 621, A92
Santoliquido F., Mapelli M., Giacobbo N., Bouffanais Y., Artale M. C., 2021, MNRAS, 502, 4877
Santoliquido F., Mapelli M., Iorio G., Costa G., Glover S. C. O., Hartwig T., Klessen R. S., Merli L., 2023, MNRAS, 524, 307
Sargent M. T., Bé thermin M., Daddi E., Elbaz D., 2012, ApJ, 747, L31
Scannapieco E., Schneider R., Ferrara A., 2003, ApJ, 589, 35
Scannapieco E., Madau P., Woosley S., Heger A., Ferrara A., 2005, ApJ, 633, 1031
Schiminovich D. et al., 2005, ApJ, 619, L47
Schneider F. R. N. et al., 2018, Science, 359, 69
Schulze S. et al., 2024, A&A, 683, A223
Sibony Y. et al., 2024, Grids of stellar models with rotation VIII: Models from 1.7 to 500 $M_{\odot}$ at metallicity $Z = 10^{-5}$, preprint (arXiv:2407.06739), https://arxiv.org/abs/2407.06739
Smartt S. J., Eldridge J. J., Crockett R. M., Maund J. R., 2009, MNRAS, 395, 1409
Smidt J., Whalen D. J., Chatzopoulos E., Wiggins B., Chen K.-J., Kozyreva A., Even W., 2015, ApJ, 805, 44
Smith N., 2014, ARA&A, 52, 487
de Souza R. S., Ishida E. E. O., Whalen D. J., Johnson J. L., Ferrara A., 2014, MNRAS, 442, 1640
Spera M., Mapelli M., 2017, MNRAS, 470, 4739
Spera M., Mapelli M., Bressan A., 2015, MNRAS, 451, 4086
Spera M., Giacobbo N., Mapelli M., 2016, Mem. Soc. Astron. Ital., 87, 575
Stevenson S., Sampson M., Powell J., Vigna-Gó mez A., Neijssel C. J., Szécsi D., Mandel I., 2019, ApJ, 882, 121

Strolger L.-G. et al., 2015, ApJ, 813, 93
Takahashi K., Yoshida T., Umeda H., Sumiyoshi K., Yamada S., 2015, MNRAS, 456, 1320
Takahashi K., Yoshida T., Umeda H., 2018, ApJ, 857, 111
Tang J., Bressan A., Rosenfield P., Slemer A., Marigo P., Girardi L., Bianchi L., 2014, MNRAS, 445, 4287
Tanikawa A., 2024, Rev. Mod. Plasma Phys., 8, 13
Tanikawa A., Kinugawa T., Yoshida T., Hijikawa K., Umeda H., 2021, MNRAS, 505, 2170
Tanikawa A., Moriya T. J., Tominaga N., Yoshida N., 2023, MNRAS, 519, L32
Umeda H., Nomoto K., 2001, ApJ, 565, 385
Venditti A., Bromm V., Finkelstein S. L., Graziani L., Schneider R., 2024, MNRAS, 527, 5102
Vink J. S.ed. 2015, Astrophysics and Space Science Library, Vol. 412, Very Massive Stars in the Local Universe. Springer International Publishing, Switzerland
Vink J. S., de Koter A., Lamers H. J. G. L. M., 2000, A&A, 362, 295
Vink J. S., de Koter A., Lamers H. J. G. L. M., 2001, A&A, 369, 574
Vink J. S., Muijres L. E., Anthonisse B., de Koter A., Gräfener G., Langer N., 2011, A&A, 531, A132
Vink J., Higgins E., Sander A., Sabhahit G. N., 2021, MNRAS, 504, 146
Walborn N. R. et al., 2014, A&A, 564, A40
Weinmann S. M., Lilly S. J., 2005, ApJ, 624, 526
Whalen D. J., Fryer C. L., Holz D. E., Heger A., Woosley S. E., Stiavelli M., Even W., Frey L. H., 2012, ApJ, 762, L6
Whalen D. J. et al., 2013, ApJ, 777, 110
Whalen D. J., Smidt J., Even W., Woosley S. E., Heger A., Stiavelli M., Fryer C. L., 2014, ApJ, 781, 106
Wiggins A. I., Bovill M. S., Strolger L.-G., Stiavelli M., Bowling C., 2024, Kindling the First Stars II: Dependence of the Predicted PISN Rate on the Pop III Initial Mass Function, preprint (arXiv:2402.17076)
Winch E. R. J., Vink J. S., Higgins E. R., Sabhahit G. N., 2024, MNRAS, 529, 2980
Wise J. H., Abel T., 2005, ApJ, 629, 615
Woosley S. E., 2017, ApJ, 836, 244
Woosley S. E., Heger A., 2021, ApJ, 912, L31
Woosley S. E., Blinnikov S., Heger A., 2007, Nature, 450, 390
Xing Q.-F. et al., 2023, Nature, 618, 712
Yaron O., Gal-Yam A., 2012, PASP, 124, 668
Yoon S.-C., Dierks A., Langer N., 2012, A&A, 542, A113
Ziegler J. J., Edwards T. D. P., Suliga A. M., Tamborra I., Horiuchi S., Ando S., Freese K., 2022, MNRAS, 517, 2471
de Jager C., Nieuwenhuijzen H., van der Hucht K. A., 1988, A&AS, 72, 259
de Souza R. S., Ishida E. E. O., Johnson J. L., Whalen D. J., Mesinger A., 2013, MNRAS, 436, 1555
van Loon J. T., Cioni M. R. L., Zijlstra A. A., Loup C., 2005, A&A, 438, 273

APPENDIX A: HE CORE MASS CRITERION

In this section, we explore how adopting the criterion on $M_{\rm He}$, instead of $M_{\rm CO}$, affects our results. We impose that only stars with $M_{\rm He}$ in the range [64–135] $M_\odot$ explode as PISNe, as adopted in SEVN (Spera & Mapelli 2017). We consider [70–120] and [60–140] $M_\odot$ as pessimistic and optimistic ranges, respectively, based on previous works (see references in Section 2.2). Table A1 shows the stellar

Table A1. As in Table 2, with $M_{\rm He}$ mass ranges and, consequently, different $Z_{\rm max}$.

Name	Stellar code	$M_{\rm He}/M_\odot$	$M_{\rm up}/M_\odot$	$Z_{\rm max}$
P	FRANEC	70–120	150	1.5×10^{-3}
M1	PARSEC-I	64–135	150	2.0×10^{-3}
M2	FRANEC	60–140	150	3.1×10^{-3}
F	PARSEC-I	64–135	300	7.9×10^{-3}
M3	PARSEC-II	60–140	150	8.7×10^{-3}
O	PARSEC-II	60–140	300	1.5×10^{-2}

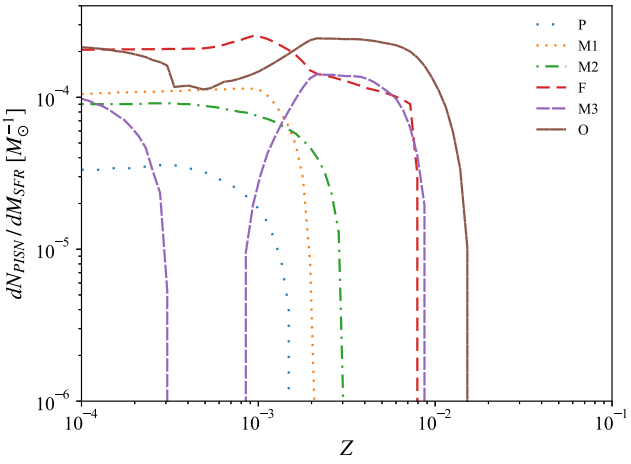

Figure A1. As in Fig. 5, using the $M_{\rm He}$ criterion (see Table A1).

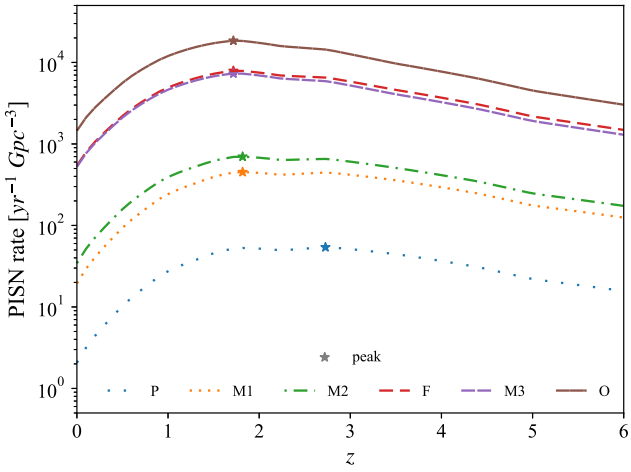

Figure A2. As in Fig. 6, using the $M_{\rm He}$ criterion.

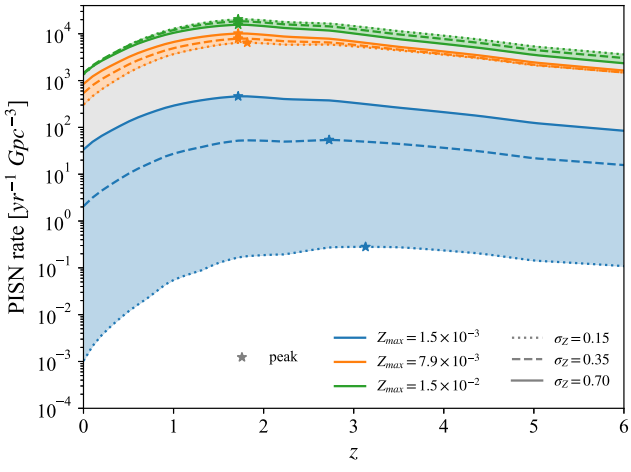

Figure A3. As in Fig. 8, using the $M_{\rm He}$ criterion.

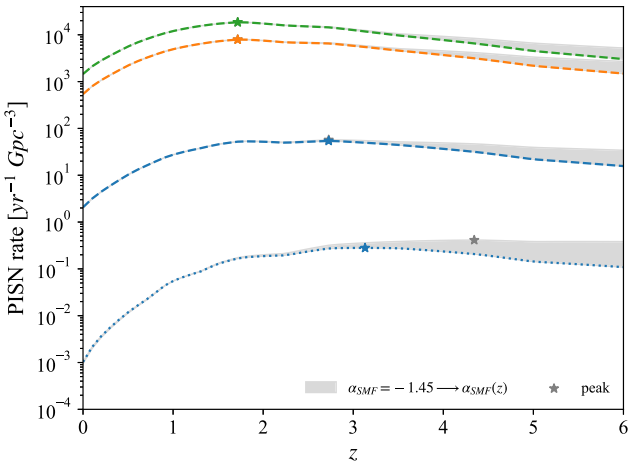

Figure A4. As in Fig. 9, using the $M_{\rm He}$ criterion.

variations we considered, namely the same as in Table 2 but with $M_{\rm He}$ ranges. Note that $Z_{\rm max}$ is modified as a consequence.

As shown in Fig. A1, the shape of $\mathrm{d}N_{\rm PISN}/\mathrm{d}M_{\rm SFR}$ is similar to the $M_{\rm CO}$ case (Fig. 5), except for variation $M3$, which exhibits a harsh drop at metallicities between ~ 4 and 9×10^{-3}. This is due to envelope undershooting, reducing the mass of the core and thus preventing stars in the corresponding mass range from going into PISN. The effect on $M_{\rm He}$ is stronger than on $M_{\rm CO}$, where it manifests as a softer drop. See Costa et al. (2021) for a detailed explanation of this process in PARSEC. We note that this drop is not particularly relevant for the PISN rate, the main contribution coming from the bulge between $Z \sim 2 \times 10^{-3}$ and 7×10^{-2}. $Z_{\rm max}$ is affected in a non-negligible way in most variations, as shown in Table A1. The values of $\mathrm{d}N_{\rm PISN}/\mathrm{d}M_{\rm SFR}$ change by some small factor. Note that we chose core mass ranges which are not correspondent to each other, between the $M_{\rm CO}$ and $M_{\rm He}$ cases, which is mostly causing these differences.

In Fig. A2, we show the PISN rate resulting from each stellar variation. As one can see, the rates only change by some small factor, in any case less than one order of magnitude, mainly due to the different $Z_{\rm max}$ (compare with Fig. 6). In particular, variations P and O are not subject to dramatic changes, so that the range of results is left substantially unaffected.

Analogously, we find that also applying our galactic variations does not lead to significant differences, with the PISN rate ranges being only slightly shrinked with respect to the $M_{\rm CO}$ case, as shown in Figs A3 and A4.

Overall, we find that varying between $M_{\rm CO}$ and $M_{\rm He}$ criterion does not change our results significantly.

APPENDIX B: ADDITIONAL IMF UPPER LIMIT VARIATION

Throughout this work, for simplicity we assumed a Kroupa IMF, and explored variations on its upper limit, $M_{\rm up} = 150$ and $300\,\mathrm{M}_\odot$. Extending this IMF to higher masses does not affect our results significantly. In order to prove this point, we consider an additional variation with $M_{\rm up} = 600\,\mathrm{M}_\odot$.

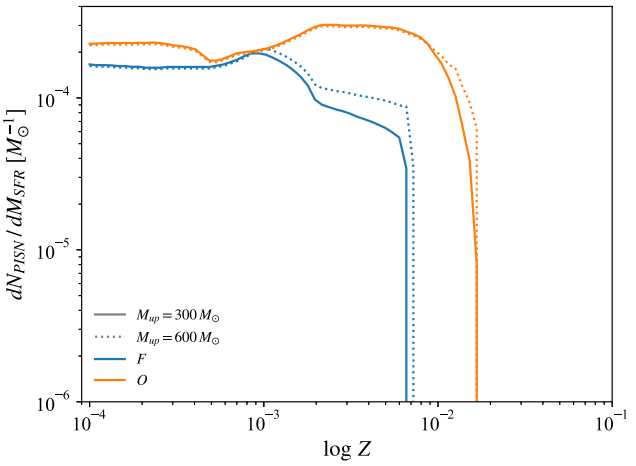

Figure B1. As in Fig. 5, for $M_{\rm up} = 300$ and $600\,\mathrm{M}_\odot$ (solid and dotted lines, respectively), and for $M_{\rm CO} \in [60 - 105]$ and $[45, 120]\,\mathrm{M}_\odot$ (F and O in the legend). The PARSEC-II stellar evolution tracks have been employed.

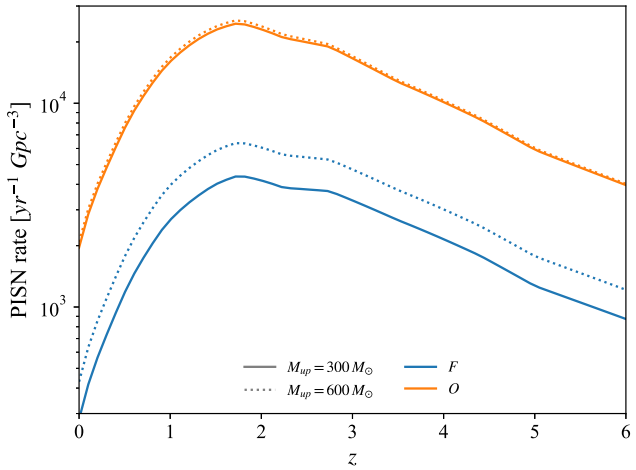

Figure B2. PISN rate as a function of redshift, obtained with the PARSEC-II tracks for the stellar variations shown in Fig. B1. Galactic parameters are fixed to $\sigma_{\rm Z} = 0.35$ and $\alpha_{\rm SMF} = -1.45$.

Indeed, considering the typical $M_{\rm ZAMS}$ of $\sim [140, 260]\,\mathrm{M}_\odot$ for PISN progenitors, one would not expect IMFs with $M_{\rm up} > 260\,\mathrm{M}_\odot$ to have any effect. However, the stellar evolution codes we consider here produce $M_{\rm ZAMS}$ ranges varying significantly with metallicity, as shown in Table 1. In particular, they predict even VMSs beyond $300\,\mathrm{M}_\odot$ to end their life as PISN, at high metallicity. Therefore, in principle extending the IMF to $600\,\mathrm{M}_\odot$ could play a role.

Among our set of stellar variations, we select F and O, since they have respectively the lowest and highest $Z_{\rm max}$ among all possible variations with $M_{\rm up} = 300\,\mathrm{M}_\odot$. For simplicity, we do not consider different variations on $M_{\rm CO}$, which do not play a significant role in this case. Fig. B1 shows the $\mathrm{d}N_{\rm PISN}/\mathrm{d}M_{\rm SFR}$, we obtain by imposing $M_{\rm up} = 300$ and $600\,\mathrm{M}_\odot$. In variation O, setting $M_{\rm up}$ to $600\,\mathrm{M}_\odot$ has

an appreciable effect only at $Z \gtrsim 10^{-2}$, where it slightly increases $\mathrm{d}N_{\mathrm{PISN}}/\mathrm{d}M_{\mathrm{SFR}}$. In variation F, $\mathrm{d}N_{\mathrm{PISN}}/\mathrm{d}M_{\mathrm{SFR}}$ gets increased starting from $Z \lesssim 10^{-3}$, and also Z_{max} is slightly higher. As one can see in Fig. B2, the effects on the PISN rate are negligible for variation O, while in variation F the rate is increased only by a small factor, between 1 and 2. This is because in the first case Z_{max} is greater than the SFRD peak (see Section 2.1), therefore the main contribution to the PISN rate is already included. In variation F, Z_{max} is lower than the SFRD peak, so the rate is more sensible to this variation, even though it is affected only in a minor way.

All in all, we find that varying M_{up} from 300 to 600 $\mathrm{M}_{\odot}$ does not have a significant effect on the PISN rate. This is due to the fact that our Kroupa IMF prescribes a low number of stars with mass between 300 and 600 $\mathrm{M}_{\odot}$. Adopting a more top-heavy IMF might lead to different results.

This paper has been typeset from a TEX/LATEX file prepared by the author.